

Generation of Higher Order Laser Beams Using a Spatial Light Modulator

Bachelor thesis in physics

by

Natalija Rajeshri Sheth

presented to the faculty of physics, mathematics and computer science (FB 08)
at the Johannes Gutenberg Universität Mainz
on September 02, 2021

First supervisor: Prof. Dr. Patrick Windpassinger
Second supervisor: Prof. Dr. Ferdinand Schmidt-Kaler

Declaration of authorship

Hereby, I assure that I wrote this thesis myself. I did not use any other sources than the ones indicated and that quotes are referred to as such.

Mainz, September 02, 2021

.....

Natalija Rajeshri Sheth
AG QOQI
Institut für Physik
Staudingerweg 7
Johannes Gutenberg-Universität D-55128 Mainz
nsheth@students.uni-mainz.de

Abstract

Higher order laser modes such as Laguerre-Gaussian (LG) beams have proved to be of great interest in physics since they carry orbital angular momentum (OAM). OAM provides an additional degree of freedom which can be controlled and, for example, be used to transport information in quantum communication. Nevertheless, most commonly lasers have a Gaussian intensity profile and do not carry OAM. In this thesis, LG beams are generated by using a phase-only spatial light modulator (SLM). However, it is known that achieving high mode purity for an optical mode cannot be done by solely modulating the phase of the beam, but requires amplitude modulation as well. We will therefore implement an algorithm that enables simultaneous control of phase and amplitude of a complex wave field of a beam using a single, phase-only SLM. The resulting beam profiles of the generated optical modes will be examined and compared to the theoretically predicted beam profiles. To make this comparison, we will evaluate parameters which characterize the donut-like LG mode, such as inner and outer radii and beam waist.

Acknowledgements

At this point, I would like to thank everybody who supported me during my work in this thesis.

First of all, I would like to thank Prof. Dr. Patrick Windpassinger for giving me the opportunity to write my thesis in the QOOI group and for his great flexibility as well as his helpful advice.

I would like to thank Prof. Dr. Ferdinand Schmidt-Kaler for kindly agreeing to be second supervisor of my thesis.

Thanks to the research group Optical Technologies and Photonics from TU Kaiserslautern led by Prof. Dr. Georg von Freymann for providing us the Python script that we used to transmit the bitmap to the SLM.

Moreover, I wish to thank Ishan Varma for introducing me to the topic and to the laboratory work. I am very grateful that he always took the time to answer all my uprising questions and to proofread my thesis several times.

I also want to express my gratitude to Sören Boles and André Wenzlowski for proofreading and for helpful annotations to improve my thesis.

Finally, I would like to thank my family and friends for their mental support and for listening to all my troubles.

Contents

1. Introduction	2
2. Theoretical Background	4
2.1. The Paraxial Wave Equation	4
2.2. Solutions of the Paraxial Wave Equation	5
2.2.1. Gaussian Beams	5
2.2.2. Laguerre-Gaussian Beams	6
2.3. $1/e^2$ Beam Width	7
2.3.1. Knife Edge Measurement	7
3. Introduction to phase-only Spatial Light Modulators	11
3.1. Liquid crystals	11
3.2. Setup of spatial light modulators	12
3.3. Working principle of spatial light modulators	13
4. Phase-only modulation using proprietary software	15
4.1. Corrections	16
4.2. Grating	16
5. Implementation of a Phase and Amplitude Modulating Algorithm	18
5.1. Working Principle	18
5.2. Angular Plane Wave Spectrum Method	20
5.3. Description of the implemented code	21
5.4. Simulations	23
6. Measurements and Experimental Results	25
6.1. Experimental Setup	25
6.2. Beam dimensions of the incident beam	26
6.3. Diffraction efficiency of the Gratings	28
6.4. Examination of the Purity of the Modes	30
6.4.1. Beam waist of the Modes	33
6.4.2. Inner and Outer radii of the LG modes	35
7. Conclusion and Outlook	48
A. Fitting methods and mathematics	49
A.1. Generalized Laguerre polynomials	49
A.2. Weighted Mean value	49
A.3. Fitting methods	49

B. Additional Figures	50
B.1. Pictures from the beam profiling camera	50
B.2. Plots of the line profiles	51
C. Matlab code	55

1. Introduction

The proposition that light itself is composed by quantised units of energy, called photons, was put forth by Einstein over a century ago [22]. A photon is a quantum of light that carries a specific amount of energy. Hence, properties such as energy, momentum and angular momentum which are known to be continuous in mechanics are discretised in quantum mechanics.

Laser beams are created by the stimulated emission of such photons [4]. Thus, the light of laser beams has a well-defined energy and frequency. Because of these properties, lasers are used in many physical applications like atom trapping [17], spectroscopy for analyzing atoms and molecules [5], or in microscopy to study the surface of various substances in detail without destroying them [3]. It is known that beyond the fundamental Gaussian beams, there are modes which carry topological information, like Orbital Angular Momentum (OAM). Such beams are called OAM beams and have found wide ranging applications in many fields, ranging from microscopy to particle manipulation [20]. For example, the performance of optical tweezers, which are used for particle manipulation and trapping, can be improved by using higher order optical modes [21]. The topological complexity and information in OAM beams can also be increased by modulating the local polarization of light. This degree of freedom is called the Spin Angular Momentum (SAM) of light and the corresponding beams are referred to as Optical Vector (OV) beams.

The QOQI (Experimental Quantum Optics And Quantum Information) research group at the Johannes Gutenberg Universität Mainz is part of the TopDyn (Transfer of Topological properties of light to Matter) Excellence project. In this project, the strategy is to induce topological properties into Quantum Matter by transferring the topological properties of OAM and OV beams to a sample of ultracold atomic gas and study the dynamics of such a system.

Most common lasers have a Gaussian intensity profile [24]. In general, there are two methods used to create OAM and OV beams: either using diffractive optical elements (DOE) or spatial light modulators (SLM). DOEs are optical elements used to modulate the phase of a light beam by etching microscopic patterns on the surface [13]. This pattern causes different points on a light beam to undergo unequal phase retardations when incident on the DOE. A disadvantage of using DOEs is that one will need to manufacture a different DOE every time a new phase retardation pattern is required. In contrast, SLMs are more flexible [2]: the phase delays that are imparted to the beam are defined by a digital hologram. Therefore, by changing the digital hologram displayed on the SLM, it is possible to arbitrarily modulate a light beam.

The aim of this thesis was to use a Spatial Light Modulator (X15213-01, *Hamamatsu Photonics GmbH*), for the generation of a class of OAM beams called Laguerre Gaussian (LG) modes with high mode purity. LG modes as solutions of the paraxial wave

equation will be introduced in Chapter 2 which deals with the theoretical background of some concepts relevant to this thesis. An introduction to spatial light modulators (SLMs) can be found in chapter 3. Here, we will discuss the various components of an SLM and also their working principles. In Section 4, we will present the different steps involved in phase-only modulation of a light beam. These include the use of look-up-tables, correction patterns and diffraction gratings.

In [27], an algorithm is presented that enables simultaneous phase and amplitude modulation of a complex wave field using a single phase-only SLM. The motivation behind implementing this algorithm is to increase the purity of our generated optical modes. The algorithm was coded in MATLAB and is described in Chapter 5. There, we will also consider simulations to get an idea of the functioning of the algorithm. In Section 6, we use the algorithm in our experiment and evaluate its performance. Knife edge measurements to estimate the radius of our laser beam are also presented in this section. Finally, we perform a purity analysis for the generated optical modes to evaluate the performance of the algorithm.

2. Theoretical Background

The electromagnetic radiation in laser beams is created by the stimulated emission of photons which is then amplified by a resonator [4]. We will attempt to derive the oscillation of electric field associated with that electromagnetic radiation. In this section, we will introduce the paraxial wave equation and discuss some properties of Gaussian and Laguerre-Gaussian modes, which are solutions of the paraxial wave equation. During the course of this thesis, we have mainly dealt with these two classes of optical modes.

2.1. The Paraxial Wave Equation

In our experiment, we use laser beams which are solutions of the paraxial wave equation. In this section, we will derive the paraxial wave equation and show how it can be used to describe the properties of laser beams. We basically follow the derivation used in [12].

Laser light is a form of electromagnetic radiation and therefore, the electric and magnetic field oscillations associated with it can be described as a solution of the classical wave equation. The electric field, $E(\vec{x}, t)$, for example, satisfies,

$$\nabla^2 E(\vec{x}, t) = \frac{1}{c^2} \frac{\partial^2 E(\vec{x}, t)}{\partial t^2}, \quad (1)$$

with the speed of light c . For monochromatic waves, such as laser beams, we can use the method of separation of variables to write the solution for $E(x, t)$ as,

$$E(\vec{x}, t) = E(\vec{x})e^{i\omega t}, \quad (2)$$

in complex notation with the complex amplitude $E(\vec{x}) = |E|e^{i\phi(\vec{x})}$ and the radial frequency ω . We then substitute for $E(\vec{x}, t)$ in Equation 1 which yields

$$\frac{1}{E(\vec{x})} \nabla^2 E(\vec{x}) = \frac{1}{c^2 e^{i\omega t}} \frac{\partial^2}{\partial t^2} e^{i\omega t}. \quad (3)$$

The right side of the equation can be solved easily. By using the definition of the wave number $k = \frac{\omega}{c}$, it results in

$$\frac{1}{c^2 e^{i\omega t}} \frac{\partial^2}{\partial t^2} e^{i\omega t} = - \left(\frac{\omega}{c} \right)^2 = -k^2. \quad (4)$$

With that, we can rewrite Equation 3 in the following manner,

$$(\nabla^2 + k^2)E(\vec{x}) = 0, \quad (5)$$

which is known as the *Helmholtz equation* [23].

Now consider waves propagating in z -direction. The complex amplitude of such waves is given by

$$E(\vec{x}) = A(\vec{x}) e^{-ikz}, \quad (6)$$

with $A(\vec{x})$ being the transverse profile of the wave. Inserting this into the Helmholtz equation gives us

$$\nabla^2 A(\vec{x}) - 2ik \frac{\partial A(\vec{x})}{\partial z} = 0. \quad (7)$$

In Equation 6, we assumed that the wave is propagating along the z -axis. We can assume that the decay of intensity in z -direction is small compared to decay in the x - and y -direction [8]. Hence, within a propagation of λ , the variation of $A(\vec{x})$, i. e. the derivative of A with respect to z , is smaller than $A(\vec{x})$ itself, meaning

$$\frac{\partial A(\vec{x})}{\partial z} \ll \frac{A(\vec{x})}{\lambda} = \frac{k A(\vec{x})}{2\pi} \ll k |A(\vec{x})|, \quad (8)$$

where $k = \frac{2\pi}{\lambda}$ was used. Consequently, the second derivative of $A(\vec{x})$ with respect to z satisfies

$$\frac{\partial^2 A(\vec{x})}{\partial z^2} \ll k \frac{\partial A(\vec{x})}{\partial z} \ll k^2 A(\vec{x}). \quad (9)$$

For that reason, we can neglect the term $\frac{\partial^2 A(\vec{x})}{\partial z^2}$ in Equation 7. With that approximation, we get the *paraxial wave equation*,

$$(\nabla_t^2 - 2ik)A(\vec{x}) = 0, \quad (10)$$

where $\nabla_t^2 := \frac{\partial^2}{\partial x^2} + \frac{\partial^2}{\partial y^2}$.

2.2. Solutions of the Paraxial Wave Equation

There are various classes of solutions to the paraxial wave equation. One can also refer to these solutions as *optical modes*. For the context of this thesis, Gaussian and Laguerre-Gaussian modes are of particular interest.

2.2.1. Gaussian Beams

For solving Equation 10, we use the ansatz

$$A(\vec{x}) = \frac{A}{q(z)} e^{ik \frac{x^2+y^2}{2z}}, \quad (11)$$

with the wave number k and a constant A and the definition

$$\frac{1}{q(z)} = \frac{1}{R(z)} - i\frac{\lambda}{\pi w^2(z)}, \quad (12)$$

with the radius of curvature and the beam radius, $R(z)$ and $w(z)$, respectively, which is known from [9]. Using Equation 6 and 2, the electric field of the Gaussian beam then can be written as,

$$E(\vec{x}, t) = A_0 \frac{w_0}{w(z)} e^{-\frac{x^2+y^2}{w(z)}} e^{-i\left(kz + \frac{x^2+y^2}{2R(z)} - \zeta(z)\right)} e^{i\omega t}, \quad (13)$$

with a phase shift $\zeta(z) = \arctan \frac{z}{z_R}$, called the *Gouy phase*. The *Rayleigh range* z_R describes the propagation distance of the beam at which the radius of the beam is $\sqrt{2}$ times as large as the initial waist w_0 . Since the intensity I is proportional to $|E|^2$, the intensity profile of a Gaussian beam is given by

$$I(x, y) = I_0 e^{-\frac{2(x^2+y^2)}{w^2(z)}}. \quad (14)$$

The beam radius $w(z)$ varies with z . It can be calculated using

$$w(z) = w_0 \sqrt{1 + \left(\frac{z}{z_R}\right)^2}, \quad (15)$$

with the *Rayleigh range* z_R .

2.2.2. Laguerre-Gaussian Beams

The paraxial wave equation in cylindrical coordinates yields another set of solution [9]. These solutions are called *Laguerre-Gaussian (LG) modes*. Mathematically, they are given by

$$U_{l,p}(r, \theta, z) = A_0 \left(\frac{\sqrt{2}r}{w(z)}\right)^l L_p^{(l)}\left(\frac{2r^2}{w^2(z)}\right) \frac{w_0}{w(z)} e^{-i\Phi_{pl}(z)} e^{i\frac{kr}{q(z)}} e^{il\theta}, \quad (16)$$

with the definition

$$\Phi_{pl} := (2p + l + 1) \arctan \frac{z}{z_R}. \quad (17)$$

The definition of $q(z)$ is given in Equation 12, and the definition of the generalized Laguerre polynomial $L_p^{(l)}$ can be found in the appendix, Section A.1. The beam waist w_0 is a measure of the transverse extent of the LG beam, similar to what we have for Gaussian beams. The index p is known as the radial order of the mode whereas l represents its azimuthal order. Since the initial beam waist w_0 increases with the propagation of the beam, it must be described by a position dependent function $w(z)$.

Like for the Gaussian beam, it increases with z .

Due to the dependence of the phase term $e^{il\theta}$ on the azimuthal order l , the wave front in an LG mode twists l times around the propagation axis and the wavefront has a helix-like structure as shown in Figure 1. This causes a phase singularity in the center. Figure 2 shows the amplitude and phase profiles of LG modes of different azimuthal orders.

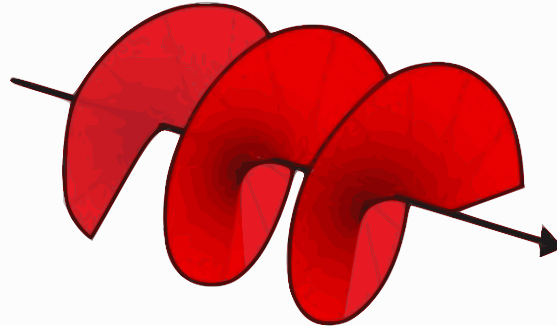


Figure 1: The wavefront of an LG mode twists around its propagation axis. The number of twists per wavelength is defined by the azimuthal order l . Illustration edited from [6].

2.3. $1/e^2$ Beam Width

In order to characterize a Gaussian beam, we will consider the radius of the beam. As described in Section 2.2.1, the radius of a beam is given by w_z . It is also referred as $1/e^2$ width since it corresponds to the distance between the intensity maximum of the beam and x_0 at which the intensity drops to $1/e^2 = 0.135$ times of the maximum. An illustration of this definition can be found in Figure 3. It shows a Gaussian beam profile and the $1/e^2$ - diameter of the profile.

2.3.1. Knife Edge Measurement

The knife edge measurement is a technique to determine the radius of a Gaussian beam. Here, a knife edge is mounted on a translation stage which is placed in the path of the beam. A schematic for this kind of measurements is sketched in Figure 4. In the beginning, the beam is allowed to propagate without obstruction. The knife edge is then moved across the beam using the translation stage. We then measure the transmitted power at various knife positions. In the following, we will derive a formula to fit the obtained data. The derivation will be based upon [12].

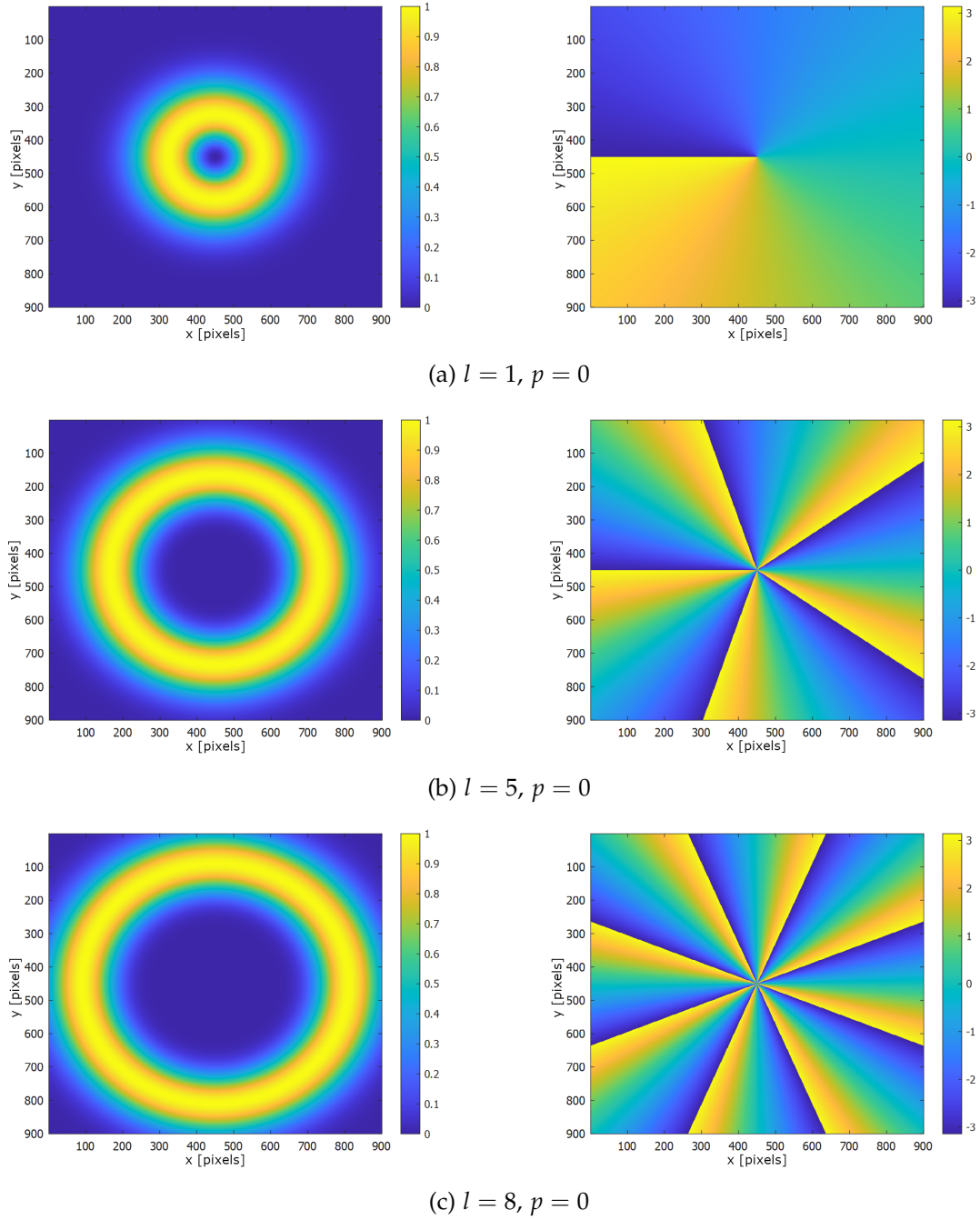


Figure 2: LG modes of different azimuthal order l . On the left, the amplitude patterns can be found. Inner and outer radii increase by increasing l . The phase pattern of each order is illustrated on the right. The number of twists corresponds to l . All patterns were generated using the code provided in [15]

Since Intensity is power received per unit area, the total power P is given by

$$P = \int_{-\infty}^{\infty} I(x, y) dx dy. \quad (18)$$

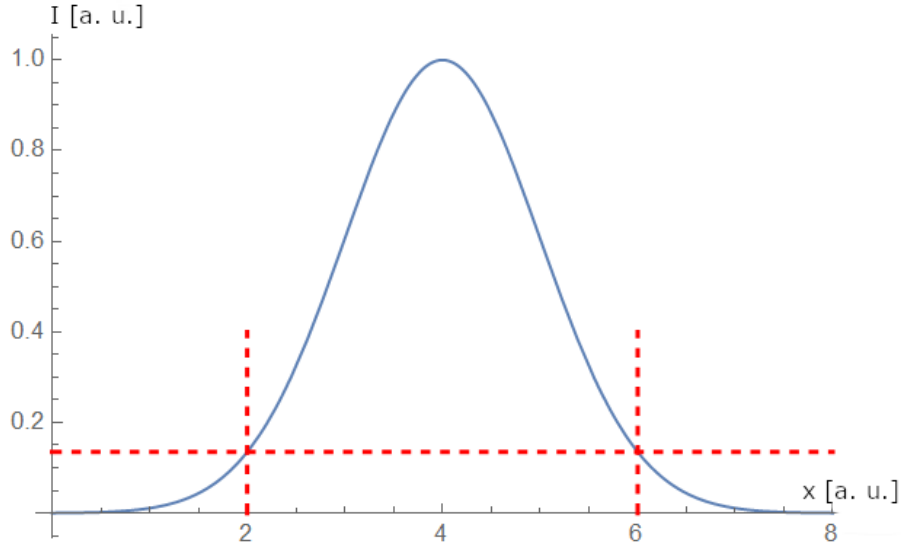


Figure 3: A Gaussian intensity profile normalized to 1. The horizontal dashed line is at $I = 0.135$. The distance between their intersection points is known as the $1/e^2$ beam diameter.

In order to accommodate possible ellipticity in our non-ideal Gaussian beam, we



Figure 4: Schematic setup of a knife edge measurement. The power within the laser beam is measured while the knife edge is moved across the beam.

assume two different radii for the beam along the x - and y - directions, w_x and w_y , respectively. Hence, the power P_{total} of the entire beam is given by

$$P_{\text{total}} = I_0 \int_{-\infty}^{\infty} e^{-\frac{2x^2}{w_x^2}} dx \int_{-\infty}^{\infty} e^{-\frac{2y^2}{w_y^2}} dy. \quad (19)$$

The above integrals can be solved by substitution. By defining

$$z := \frac{\sqrt{2}}{w_x} x, \quad (20)$$

the integral over x becomes a Gaussian integral including a constant prefactor of $\frac{w_x}{\sqrt{2}}$. The Gaussian integral is known to be $\sqrt{\pi}$ [1]. A similar substitution can also be used for the integral over y . Then, the total power P_{total} results in

$$P_{\text{total}} = I_0 \frac{\pi}{2} w_x w_y. \quad (21)$$

We define P as the transmitted power in the beam when it is partially covered by the knife edge. Mathematically, this is given by

$$P = P_{\text{total}} - \int_{-\infty}^{x'} e^{-\frac{2x^2}{w_x^2}} dx \int_{-\infty}^{\infty} e^{-\frac{2y^2}{w_y^2}} dy, \quad (22)$$

for measurement in the horizontal direction. The expression for the measurement done in the vertical direction is obtained similarly.

The integral over x in Equation 22 can be evaluated with the substitution method, as explained in Equation 20, We then have,

$$\frac{w_x}{\sqrt{2}} \int_{-\infty}^{z'} e^{-z^2} dz = \frac{w_x}{\sqrt{2}} \left(- \int_0^{-\infty} e^{-z^2} dz + \int_0^{z'} e^{-z^2} dz \right), \quad (23)$$

with $z' := \frac{\sqrt{2}}{w_x} x'$. From [1], it is known that the above integrals correspond to the definition of the error function given by

$$\text{erf}(x) = \frac{2}{\sqrt{\pi}} \int_0^x e^{-x'^2} dx', \quad (24)$$

with $\lim_{x \rightarrow \pm\infty} \text{erf}(x) = 1$. Consequently, the measured power as a function of the position x of the knife edge is given by

$$P(x) = \frac{1}{2} P_{\text{total}} \left(1 - \text{erf} \left(\frac{\sqrt{2}x}{w_x} \right) \right). \quad (25)$$

In order to consider a possible offset, the function

$$P(x) = \frac{1}{2} P_{\text{total}} \left(1 - \text{erf} \left(\frac{\sqrt{2}(x - x_0)}{w_x} \right) \right), \quad (26)$$

with the parameters P_{total} , x_0 and w_x is fitted to the measured data.

3. Introduction to phase-only Spatial Light Modulators

In general, laser beams have a Gaussian intensity profile. Higher order laser modes such as LG modes can be obtained from Gaussian beams with the help of diffractive optics. For this thesis, we use a Spatial Light Modulator (SLM) to generate the desired higher order modes.

The spatial light modulator is a phase modulating device. It modulates the phase of an incident beam such that a desired phase profile is obtained. The modulation is achieved by using liquid crystals through which the incident light is passing. Due to the properties of liquid crystals which will be described in Section 3.1, the light beam experiences phase delays. In Section 3.2, the setup of SLM is described. Here, we will also discuss the pixelated structure of the SLM screen. The working principle of the SLM will be discussed in Section 3.3.

We interface with the device using a desktop computer which makes it easy to use as well as flexible since the desired mode can be changed easily by displaying another hologram on the SLM [2].

3.1. Liquid crystals

The properties of liquid crystals are of prime importance in the working principle of spatial light modulators and are discussed in [4] and [2].

Liquid crystals are elongate molecules with no well-defined phase since they have properties of solids like anisotropy and of liquids like taking the shape of the container in which they are filled. However, liquid crystals can have three different phases depending on the temperature. At low temperatures, the liquid crystals are solid and anisotropic. By increasing the temperature, the substance becomes liquid and thus free to move but is still anisotropic. If the temperature is high enough, the anisotropy vanishes because the molecules are orientated randomly in the liquid.

In the liquid but anisotropic case, the arrangement of the liquid crystal can be either nematic, smetic or cholestric. In the nematic case, all liquid crystals are randomly distributed but have the same orientation. Smetic liquid crystals in addition are distributed in layers. A helix-like structure is called cholestric. Figure 5 illustrates the different possibilities.

In SLMs, liquid crystals are used because of their anisotropic properties. Because of anisotropy, the liquid crystal media is birefringent. Hence, the light propagating through them is divided into two beams that are orthogonally polarised to each other. A light beam polarized parallelly to the optical axis follows the Snell's law of refraction and is therefore called the *ordinary beam*, whereas the outgoing beam that is polarized vertically to the optical axis is called the *extraordinary beam*.

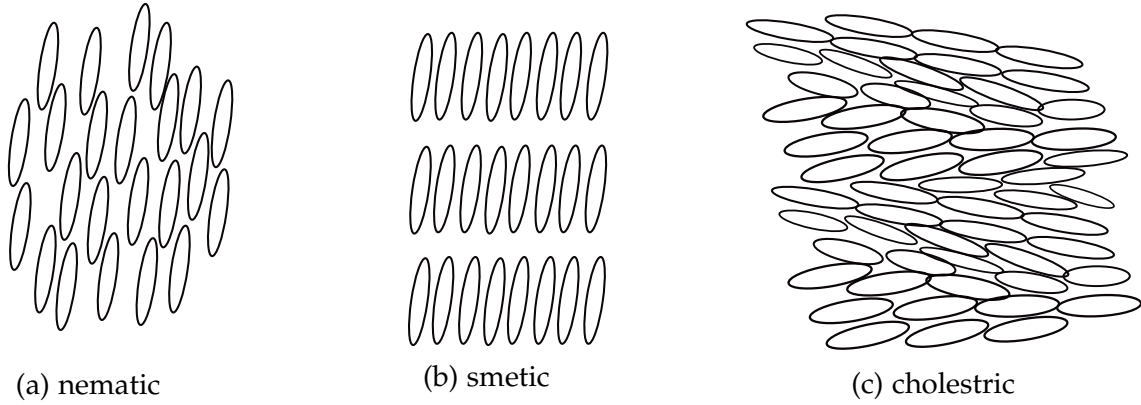


Figure 5: Illustration of the structure of liquid crystals in the liquid but anisotropic state: (a) Nematic, (b) smetic and (c) cholestric case.

This is because the refractive index of the liquid crystals, as seen by the propagating light, depends on the polarization. The refractive index of a liquid crystal can be controlled by changing its orientation with respect to the polarization of the incoming light.

Controlling the orientation of liquid crystals is possible by using voltages because the molecules form dipoles due to their elongate shape. The magnitude of the applied voltage V determines their rotation angle $\theta(V)$. According to [2], the extraordinary index of refraction becomes

$$\frac{1}{n_e^2(\theta)} = \left(\frac{\cos \theta}{n_e}\right)^2 + \left(\frac{\sin \theta}{n_o}\right)^2, \quad (27)$$

where n_o represents the ordinary index of refraction and n_e is the index of refraction for the extraordinary beam when no voltage is applied.

3.2. Setup of spatial light modulators

In our experiment, the SLM is a phase-only modulating device consisting of liquid crystals on silicon (LCOS). The setup of such a phase-only LCOS-SLM can be found in Figure 6. A computer is connected to the SLM controller. The controller transmit voltages to the SLM head via an FPC cable. The voltages are then applied to each pixel on the screen of the SLM.

Figure 7 shows the composition of the screen. A layer of nematic liquid crystals is arranged between two electrodes. The electrodes are divided into pixels. Pixels are the smallest unit of the screen which can be addressed with a unique voltage. The voltages transmitted to the SLM head are applied on the electrodes of the screen. Since they are pixelated, the screen corresponds to a pattern with discretised steps as illustrated in Figure 8. On each pixel, there are liquid crystals which are addressed with a driving

voltage.

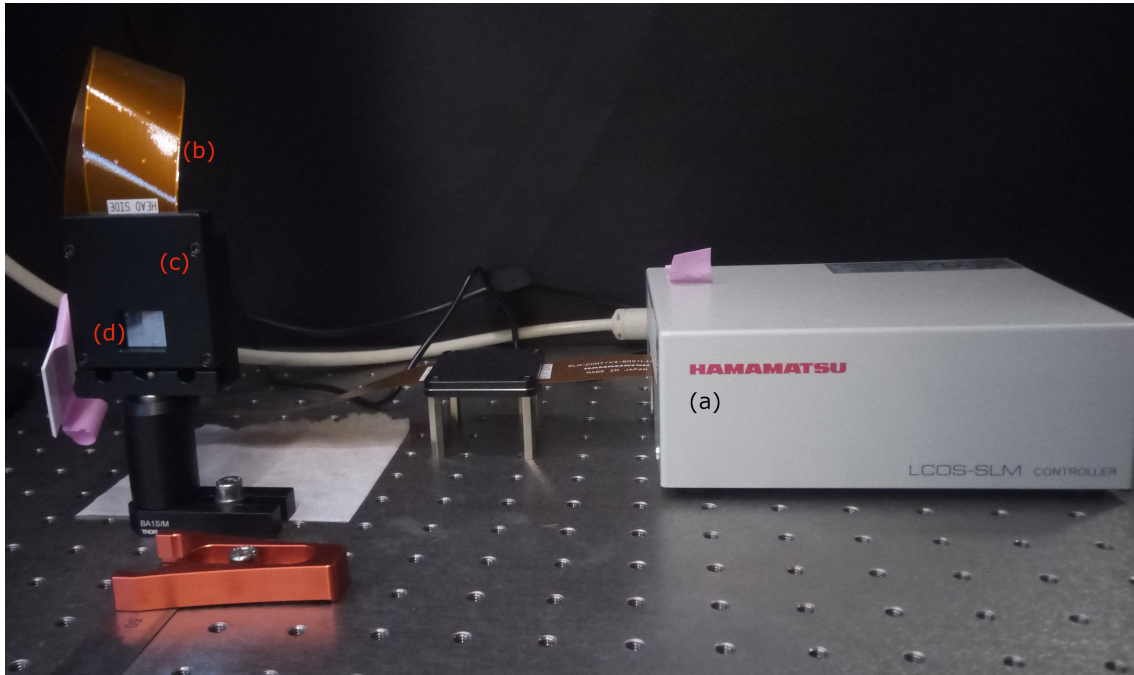


Figure 6: Picture of the SLM. The controller (a) is connected via an FPC cable (b) to the SLM head (c). In the center of the head, the screen (d) of the SLM is placed.

3.3. Working principle of spatial light modulators

The spatial light modulator is a phase modulating device. The principle of the phase modulation can be divided into three steps:

1. Generation of a bitmap representing the phase shift:

A computer is used to calculate the phase pattern which we desire to impose on the beam. Since the screen of the SLM on which the phase pattern will be displayed is pixelated, the continuous phase distribution must be discretised. Hence, we create a matrix where each component is mapped to a pixel and corresponds to some phase retardation. The phase pattern is then converted into an 8-bit grayscale image ranging from black, corresponding to the value 0, representing a phase shift of 0, to white, with a value of 255, signifying a maximal phase shift of 2π .

2. Application to the liquid crystals:

The SLM controller is connected to the same computer and is recognised as a second monitor. The bitmap image is then sent to the controller. There, it is converted into voltages that are then applied to the electrodes on each pixel of the screen. Due to these voltages, the orientation and thus the index of refraction of

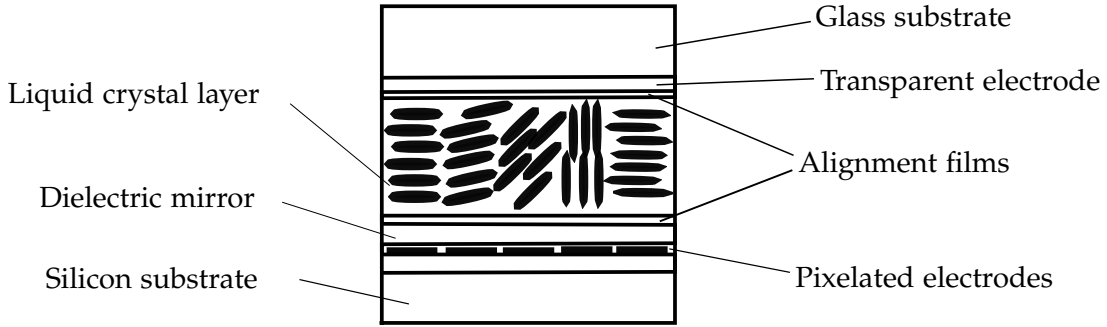


Figure 7: The SLM screen consists of different layers. Liquid crystals are between two electrodes which can be addressed on each pixel separately. By applying voltages on the electrodes, the orientation of the liquid crystals is controllable and thus also their index of refraction. A beam incident on the screen (glass substrate) is then imparted with a phase shift as defined on each pixel. The image is adapted from [10].

the liquid crystals is controllable on each pixel individually.

3. Reflection of the incident beam:

If light is incident on the screen of the SLM, it is refracted on the liquid crystals. The beam is then reflected on a dielectric mirror and passes again through the layer of liquid crystals. The incident light is polarized horizontally because of the orientation of the liquid crystals. Since the beam passes through the display twice, a larger phase range is covered [11]. This results in a phase shift of

$$\Delta\Phi = \frac{2\pi}{\lambda}d(n_e - n_o), \quad (28)$$

with the indices of refraction of the extraordinary and ordinary beam n_e and n_o , respectively, and the distance d that the beam travels through the liquid crystals. A more detailed derivation with the help of the Jones formalism can be found in [9]. As described in Equation 27, n_e depends on the rotation angle θ of the molecules which is controlled by applying voltages on the pixelated electrodes. Hence, the phase shift the incident light beam receives is defined on each pixel individually. Because of the possibility of controlling the phase retardation at each pixel individually, an SLM offers the ability to arbitrarily tailor and shape the wavefront of the light beam.

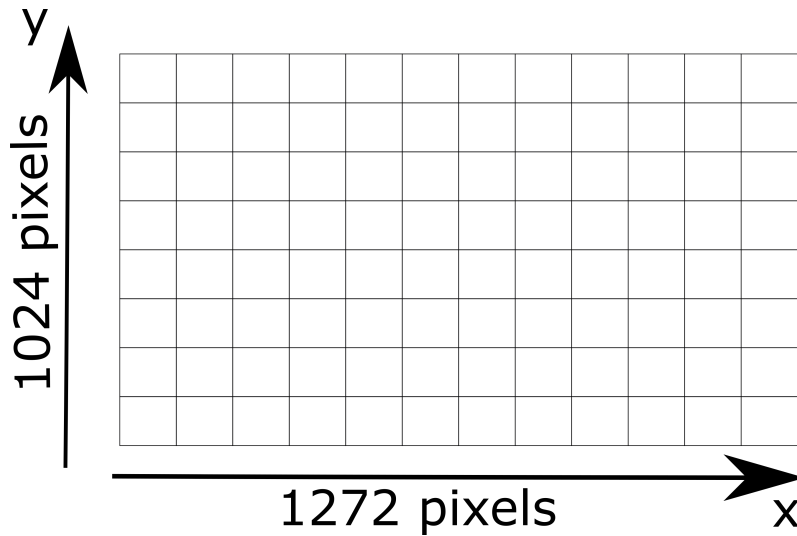


Figure 8: The screen of the SLM is pixelated. The pixels divide the screen into 1272 x 1024 units that can be addressed independently.

4. Phase-only modulation using proprietary software

The software of the SLM manufacturer *Hamamatsu Photonics GmbH* is capable of generating and displaying phase patterns on the SLM. It provides options to generate phase patterns for optical components like gratings, lenses and also higher order modes like LG beams. Furthermore, one can easily change the operating wavelength and display correction patterns using this proprietary software. Another option of the software is the use of look-up tables (LUT). LUTs are used to relate each wavelength to the specific uint8 value that results in a phase shift of 2π . In general, the bitmaps are in the range from 0 to 255. Since the phase shift in Equation 28 depends on the wavelength of the light, the voltages applied on the liquid crystals have to be adapted to obtain the same phase shift for different wavelengths.

The phase-only hologram that will be displayed on the SLM in order to modulate a Gaussian beam such that an LG mode is created in the output beam by calculating the phase pattern of the desired order. We will use this software to generate LG modes using phase-only modulation and compare them to the results obtained from the phase and amplitude modulating algorithm by evaluating their mode purity. The aforementioned algorithm will be presented in Section 5. Since we will use the holograms for the correction pattern and for the grating that the *Hamamatsu* software creates for both modulation methods, we will discuss their necessity and working principle in the following sections.

4.1. Corrections

Small unevenness occurs on the glass substrate of the SLM screen which is caused by imperfect manufacturing. In order to avoid the impact of this unevenness on the operation of the SLM, a correction pattern that compensates for the unevenness is provided in the software. For that purpose, the manufacturer performs interferometric measurements with each device individually to create the specific correction pattern. We will use this pattern for a wavelength $\lambda = 626 \text{ nm}$ in all measurements.

4.2. Grating

Gratings are used to spatially separate the incident beam from the reflected beam. Furthermore, since there are small distances between the pixels of the SLM screen, there will exist components of incident light that are not modulated after reflection [2]. If now a grating is added to the desired phase pattern, the light which is incident on the pixels, and is therefore modulated, can be spatially separated from the unmodulated parts.

The *Hamamatsu* software provides the option to generate reflective blazed phase gratings. The diffraction formula can be derived by considering two light rays as illustrated in Figure 9 as done in reference [19]. The angle α stands for the angle of incidence of the rays with respect to the perpendicular to the grating plane. With the distance d between the rays, their path difference is given by

$$\Delta s_i = d \sin \alpha . \quad (29)$$

Both rays get reflected with an angle β to the perpendicular. This causes another path difference given by

$$\Delta s_a = d \sin \beta . \quad (30)$$

Consequently, the condition for a diffraction maxima results in

$$m\lambda = d(\sin \alpha + \sin \beta) , \quad (31)$$

with the order of the maximum $m \in \mathbb{Z}$.

In general, the most intensity should be found in the zeroth order where $\beta = -\alpha$ but due to the sawtooth profile of blazed gratings, the diffraction order in which the highest intensity is observed can be changed. The *Blaze angle* θ_B is determined by the gradient of each sawtooth element of this grating and thus, it is also the angle between the perpendicular of the grating surface and the sawtooth surface. The angle of incidence θ_i and of emergence θ_a with respect to the perpendicular of the sawtooth

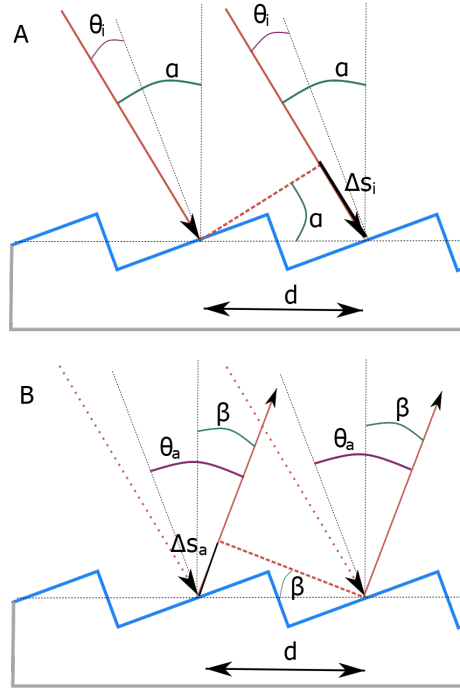


Figure 9: Illustration adapted from [19] of the reflection of a light beam on a blazed grating. In part A, two light rays are incident with an angle α with respect to the perpendicular to the grating plane and with an angle θ_i with respect to the perpendicular to the sawtooth plane. The reflection is shown in B with the angle β and accordingly θ_a .

plane can be described as

$$\theta_i = \alpha - \theta_B, \theta_a = \theta_B - \beta. \quad (32)$$

According to the reflection law, this yields the maximal intensity at the angle

$$\beta = 2\theta_B - \alpha. \quad (33)$$

Since Equation 31 also depends on the wavelength, the order of the maximum with the highest intensity is not only variable with the Blaze angle but also with the wavelength of the incident light.

In the software, the sawtooth profile is approximated by a controllable number of steps where each step corresponds to a different phase shift. The approximation is sketched in Figure 10.

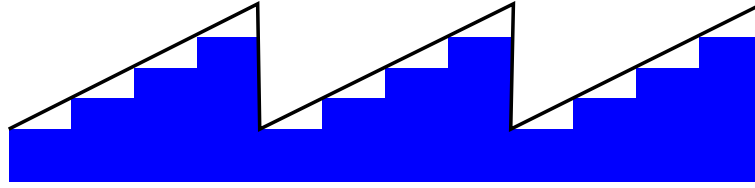


Figure 10: The sawtooth profile of the blazed grating is approximated by a controllable number of steps in the software from *Hamamatsu Photonics GmbH*. Here, the number of steps, also known as the grating number is equal to 4.

5. Implementation of a Phase and Amplitude Modulating Algorithm

The software of the manufacturer provides a large number of commonly used phase patterns as described in Section 4. However, it can only control the phase of a beam and there is no option to control the amplitude of the beam.

In [27], an algorithm that can simultaneously modulate the phase and amplitude of a laser beam with a phase-only SLM is discussed. The amplitude modulation is achieved by an iterative process where the final phase pattern which will be transmitted to the SLM is calculated from the superposition of the complex wave field of the Gaussian incident beam and the desired beam. Hence, a constraint on the amplitude can also be incorporated when calculating the phase-only hologram. A flow chart of the algorithm can be found in Figure 11. In the following sections, the individual steps will be discussed.

5.1. Working Principle

The algorithm calculates the phase hologram to be displayed on the SLM from constraints on phase and amplitude. The required input arguments are given by

- Target amplitude and phase: A_t and P_t ,
- Amplitude pattern of the incident beam a_t ,
- Initial phase shift p_0 after the first reflection from the SLM,
- Total number of iterations N and counter n .

The constraints are determined by A_t and P_t since these patterns represent the complex field we want to have after the modulation. First, the incident beam a_t is modulated with the initial phase pattern p_0 . It describes the phase shift that the beam receives after the reflection on the screen of the SLM. Mathematically, this is calculated by multiplying a_t with the corresponding exponential of the phase shift. Using a transformation method T , the beam is then propagated towards the detection plane.

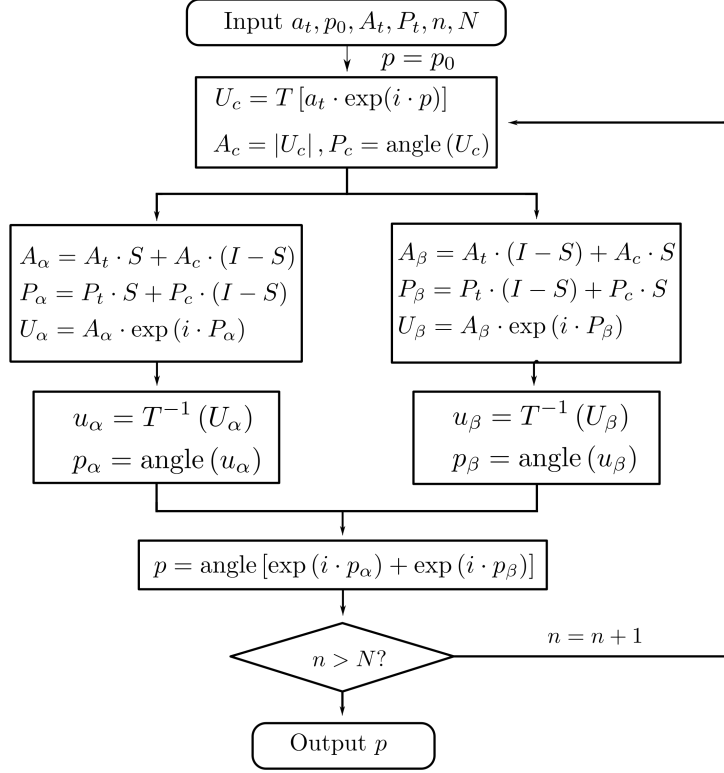


Figure 11: Flow chart of the proposed algorithm [27].

Here, the detection plane is separated into two planes α and β . In both planes, the propagated complex field, U_c , is combined with the target beam. For that purpose, two matrices I and S are defined. The dimension of both matrices correspond to the dimensions of the planes. All elements of I are 1 whereas S is populated with ones in the top half and zeros in the bottom half. In plane α , the target amplitude and phase are multiplied by S and amplitude and phase of the propagated complex field U_c are multiplied by the matrix $(I - S)$. The plane β is determined in the similar way but here, amplitude and phase of U_c are multiplied with S and the target amplitude and phase with $(I - S)$.

After having calculated the output planes α and β , the beams at both these planes are propagated backwards using the inverse transformation T^{-1} to the screen of the SLM. Here, the phase patterns of both planes, α and β , are added and the result is now the new phase pattern p that should be displayed on the SLM screen.

At this point, the iteration starts. If the counter n is smaller than the total number of iterations N , the calculation is repeated with the new phase pattern p , that was the output from the previous iteration, as the initial guess. Since the phase pattern is always replaced by the superposition of the target and propagated beam during the iteration, the propagated beam eventually converges to the target beam. After the N th iteration, the obtained phase pattern p is saved as the final phase pattern that will be

displayed on the SLM.

5.2. Angular Plane Wave Spectrum Method

The mathematical transformation we use to propagate the beam from the plane of the SLM to the detection plane is the angular plane wave spectrum (APWS) method as proposed in [24]. The derivation of the method will follow [14].

APWS is a method to model the propagation of a wave field. It involves the decomposition of an arbitrary wave into a superposition of an infinite number of plane waves. In general, a plane wave is given by

$$A(\vec{x}) = Ae^{i\vec{k}\cdot\vec{x}} \quad (34)$$

with the wave vector $\vec{k} = 2\pi\vec{f}$ where \vec{f} describes the spatial frequencies in all three dimensions.

In the beginning, a complex field $U(x, y, z)$ is evaluated at $z = 0$. At this position, the product $k_z z = 0$. Therefore, the complex field $U(x, y, 0)$ is given by the superposition of an infinite number of two dimensional plane waves. Mathematically, this yields

$$U(x, y, 0) = \int_{-\infty}^{\infty} \int_{-\infty}^{\infty} \hat{U}(f_x, f_y, 0) e^{2\pi i(f_x x + f_y y)} dx dy, \quad (35)$$

with $\hat{U}(f_x, f_y, 0)$ being the Fourier transform of the complex field at $z = 0$. Equation 35 is essentially taking an inverse Fourier transform [9].

This expression corresponds to the complex field associated with the beam directly after the modulation on the screen of the SLM in our application. We now need to know the complex field of the beam at the detection plane which is in a distance z_0 . To determine the complex field U at $z = z_0$, i. e. $U(x, y, z_0)$, we add the appropriate phase change due to propagation to each plane wave component of $U(x, y, 0)$. Thus, k_z has to be determined. The absolute value of \vec{k} is given by $|\vec{k}| = \frac{2\pi}{\lambda}$ with the known wavelength λ of the beam. Using this, k_z results in

$$k_z = \sqrt{|\vec{k}|^2 - k_x^2 - k_y^2} = 2\pi \sqrt{\left(\frac{1}{\lambda}\right)^2 - f_x^2 - f_y^2}. \quad (36)$$

After adding the appropriate phase change to the individual plane waves, we can add these plane waves together to obtain the resultant complex field U at $z = z_0$.

Mathematically, this is expressed as

$$U(x, y, z_0) = \int_{-\infty}^{\infty} \int_{-\infty}^{\infty} \hat{U}(f_x, f_y, 0) e^{2\pi i(f_x x + f_y y + z_0 \sqrt{(\frac{1}{\lambda})^2 - f_x^2 - f_y^2})} dx dy. \quad (37)$$

By denoting \mathcal{F} as the definition of the Fourier transform, the above equation can be written as

$$U(x, y, z_0) = \mathcal{F}^{-1} \left\{ \mathcal{F}\{U(x, y, 0)\}(f_x, f_y) e^{2\pi i z_0 \sqrt{(\frac{1}{\lambda})^2 - f_x^2 - f_y^2}} \right\}. \quad (38)$$

In the algorithm, discrete Fourier transforms are used since the complex field of the beam is represented by a matrix. The spatial frequencies f_x and f_y are given by

$$f_{x/y} = \frac{n_{x/y}}{L_{x/y}}, \quad (39)$$

with the length $L_{x/y}$ of the pattern in both dimensions and $n_{x/y}$ as coordinates of the individual pixels. [24].

5.3. Description of the implemented code

The algorithm is coded in MATLAB and can be found in the appendix, part C. The main file *amplitude_phase.m* calls two more functions to generate the amplitude profile of the target and incident beam. The latter is just an elliptical Gaussian profile with beam dimensions obtained from knife edge measurements that will be presented in 6.2. However, using the optional input argument '*radius*', it is possible to change the radii of the incident beam. The program *input_pattern.m* calculates this incident beam profile and normalizes it to 1.

In our case, target amplitude and phase pattern, A_t and P_t , respectively, represent LG modes. The desired radial order, r , and azimuthal order, l , are required as input arguments. There are two possibilities to generate the patterns:

1. The target patterns can be created using the OTSLM toolbox which is presented in [15]. It is a repository of various MATLAB codes to generate phase and amplitude patterns for commonly used optical modes. Here, the function *lgmode.m* is used to create the target amplitude and phase pattern for an LG mode. It calculates the patterns from the theoretical expression for the complex wave field of an LG mode according to Equation 16.
2. In Reference [24], LG modes are created by multiplying the Gaussian amplitude pattern which is incident on the SLM screen by an exponential $e^{il\theta}$. The resulting complex amplitude field is then propagated towards the detection plane using the APWS method. Amplitude and phase pattern of this propagated field are then used as target amplitude and phase pattern, respectively.

We will evaluate the performance of both methods in Section 5.4.

All amplitude patterns are normalized to 1 and the phase patterns are shifted in the

range from $-\pi$ to π .

The initial guess of the phase pattern p_0 representing the initial phase shift is generated as a random matrix in the range from $-\pi$ to π .

The transformation T is performed by calling the code *apws.m*. Its basic structure and functioning is described in Section 5.2. Since it requires the wavelength λ of the incident laser beam as well as the distance z between the screen of the SLM and the detection plane, these two variables also are input arguments of the main file.

However, the distance z is not an obligatory input argument because the experimental setup and thus the propagation distance is fixed in general. Unless explicitly changed by the user, the default value is set to $z = 600$ mm.

In order to determine the planes α and β , the matrices I and S are defined. Here, S consists of only 1s in the upper and 0s in the lower half. Figure 12 illustrates the amplitude patterns of both planes in the first iteration. The inverse transformation T^{-1} is performed by the same method, *apws.m*, but with the distance argument being negative.

The iteration is realized using a for-loop that runs N -times. N is defined when calling

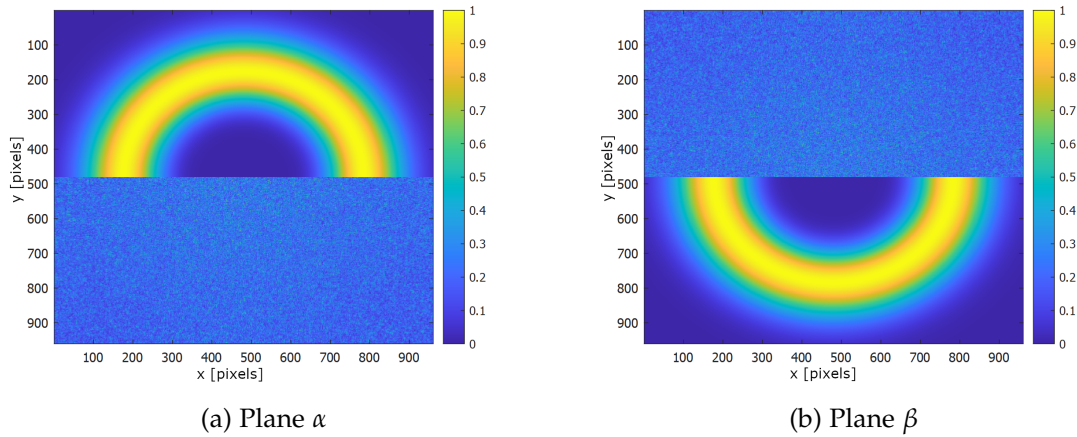


Figure 12: Amplitude patterns of plane α and β after the first iteration. The planes are complementary. In one half of each pattern, the target amplitude, a LG mode of azimuthal order of $l = 5$ is visible whereas the respective other half represents the beam after reflection from the SLM and subsequent propagation to the detection plane.

amplitude_phase.m.

After all iterations are completed, the phase pattern which is still in the range from $-\pi$ to π is shifted in the range from 0 to 2π because when converting a phase pattern to an 8-bit bitmap, 0 is mapped to 0 and 2π is mapped to 255.

In order to avoid that light from other sources affect the experiment, one can optionally create a subsection within the full SLM screen. The final phase pattern will then be displayed only in this subsection. The size of this subsection is selected so as to

completely accommodate the incident beam, avoiding any cutoffs. The size of the phase pattern can be specified either in mm or in pixels. However, the bitmaps that are displayed on the SLM need to have the same size as the screen. For this reason, we add paddings, consisting of zeros, on either side of our subsection so that the final output pattern sent to the SLM has a size of 1024×1272 pixels. A bitmap of the whole pattern is created by calling the function *create_bitmap.m* which converts the phase shifts in the interval $[0, 2\pi]$ into an 8-bit bitmap where the maximum value corresponding to 2π is 194, on a scale of 0 to 255. This value is taken from the LUT, as described in 4.1, for the wavelength $\lambda = 626$ nm which is used in the experiment.

Finally, a correction pattern for $\lambda = 626$ nm is added. It can be switched off using the option '*correction*' when calling the algorithm. The correction pattern is a bitmap created by the software of the manufacturer. In the same way, a blazed grating which can be used to spatially separate the reflected and the incident beam can be added to the phase pattern. This is specified again when calling the main file using the optional input argument '*grating*' with the grating number. The grating is created using the *Hamamatsu* software and then saved as bitmap. Both bitmaps from the *Hamamatsu* software are loaded from the algorithm and added to the phase pattern by calling the function *create_bitmap1.m*.

Using a Python script, this bitmap is displayed on the SLM.

5.4. Simulations

The calculated amplitude pattern A_c represents the output beam at the detection plane since it is essentially the beam which has propagated after the modulation towards the detection plane. Due to the iterative nature of the algorithm, it eventually converges to our target pattern. This is illustrated in Figure 13 where A_c is shown after n iterations as well as the amplitude pattern of the incident beam. It can be seen that the calculated patterns at the end retain only a small fraction of the original power in our incident beam.

As described earlier, we have two possibilities to generate the target phase and amplitude pattern. We will use both methods to create a LG beam with azimuthal order of $l = 5$.

The obtained target patterns are shown in Figure 14. The target amplitude pattern which is created as in Reference [24] is clearly smaller than the pattern generated from the OTSLM toolbox. Moreover, ringlike diffraction structures appear with this method. These should not occur for an ideal vortex beam and are undesirable for our experimental application. On the contrary, we observe no such ringlike structure when using the target amplitude generated with the OTSLM toolbox, therefore, in subsequent measurements, we decide to use the OTSLM toolbox to generate the target amplitude and phase pattern.

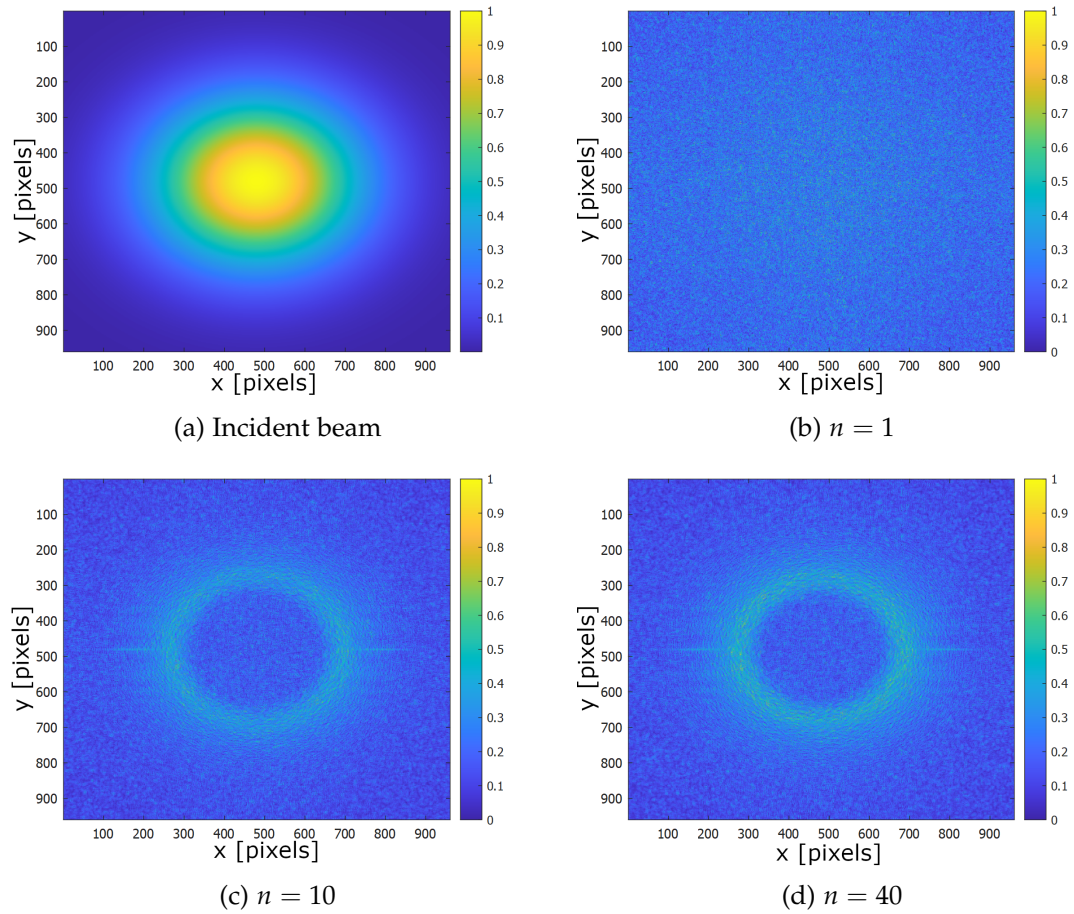


Figure 13: Amplitude patterns of the incident beam and after propagating from the SLM to the output plane after n iterations. The target pattern was a LG mode with $l = 5$, $p = 0$. After the first iteration, there is no well-defined amplitude distribution but for ten iterations, the LG mode is already visible which becomes even brighter after forty iterations.

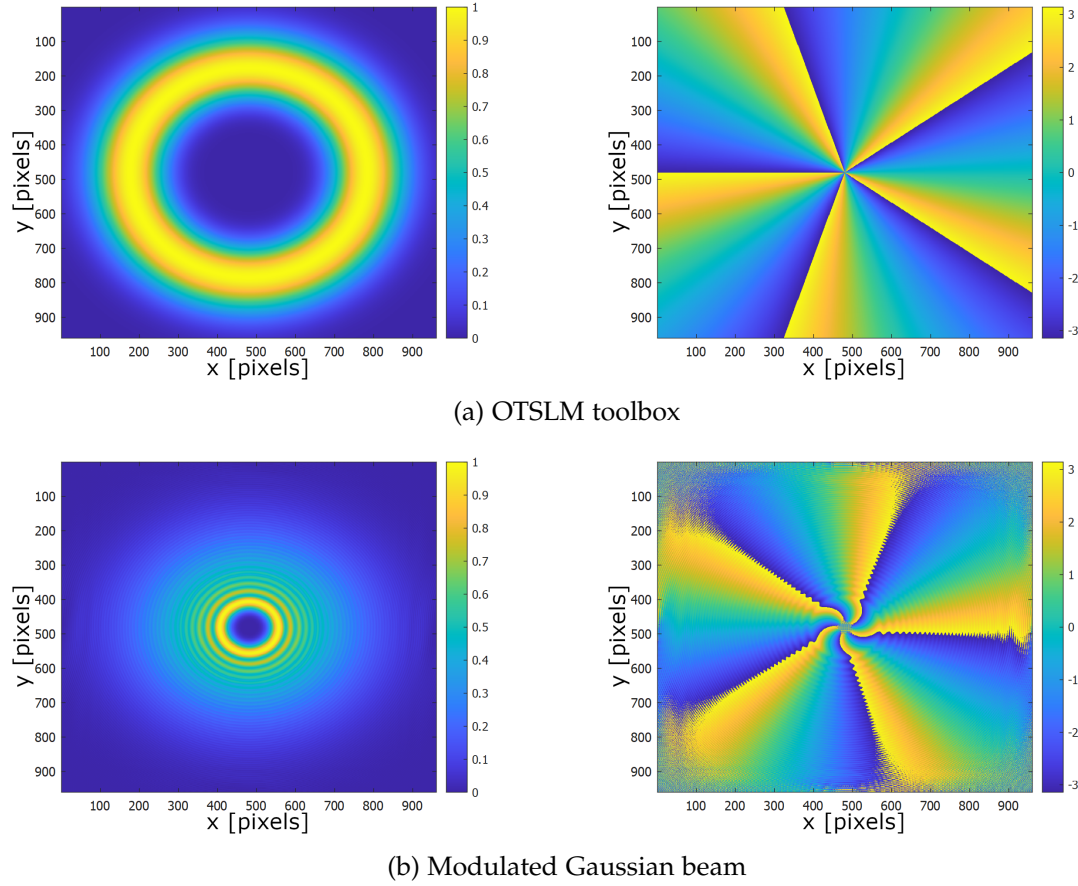


Figure 14: Amplitude (left) and phase (right) pattern of the target beam. The target beam is generated using (a) the OTSLM toolbox and (b) the method presented in [24].

6. Measurements and Experimental Results

In this section, all measurements that were performed are presented. A knife edge measurement was performed to know the beam dimensions of the incident beam which is necessary to generate its amplitude pattern. Moreover, we evaluate the diffraction efficiency for different grating numbers of the blazed grating displayed on the SLM in order to find the optimal setting for operation. Finally, the outputs of amplitude patterns we obtain after implementing the algorithm, as well as when we use the proprietary *Hamamatsu* software to generate the LG modes, are presented and are analysed using a beam profiling camera.

6.1. Experimental Setup

Laser light with wavelength $\lambda = 626$ nm is coupled into the experimental setup using a fiber coupler. The beam is then guided through a polarizing beam splitter (PBS). The

reason for that is that the SLM can modulate light with polarization only along a particular axis which is caused by the anisotropic behaviour of the liquid crystals. The beam is expanded using a telescope before being incident on the SLM. This is done in order to increase the utilization of available active area of the SLM display. Covering a larger area of the SLM screen means more pixels are being illuminated and thus, increasing the resolution with which we can modulate the phase or amplitude of our light beam. With the help of a beam profiling camera, we examine the intensity profiles of our modulated laser beams. A schematic of the experimental setup can be found in Figure 15.

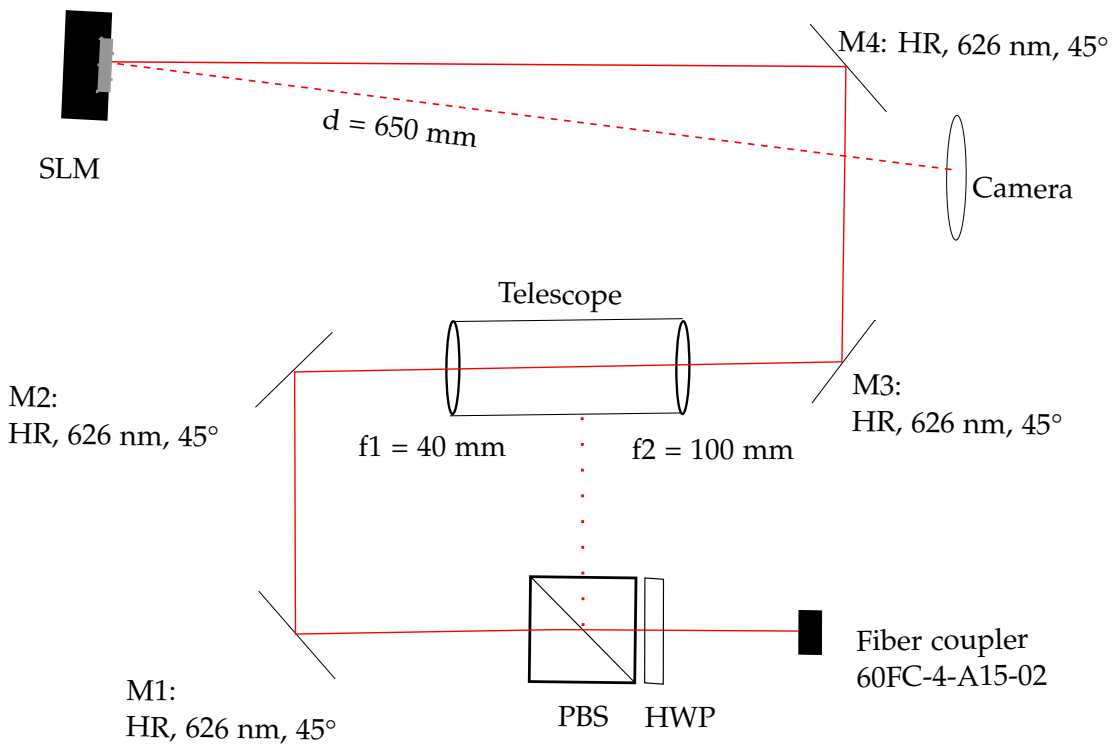


Figure 15: Schematic plot of the experimental setup. A laser beam with $\lambda = 626$ nm passes through a PBS and is then guided to the SLM with several mirrors M_i . The SLM is slightly tilted such that the beam is incident with an angle of $\alpha \approx 1.25^\circ$. The modulated beam is observed with a beam profiling camera.

6.2. Beam dimensions of the incident beam

In our experiment, the beam incident on the SLM screen has a Gaussian profile. Its exact amplitude profile, a_t , is needed in the algorithm to calculate the beam profile just after incidence on the SLM. For this purpose, it is necessary to know the beam dimensions. This is done by performing a knife edge measurement as described in Section 2.3.1.

The incident laser beam is guided through a knife edge setup after being enlarged by the telescope. It is then focused into the sensor head to measure the transmitted power. The experimental setup to measure the beam dimension in horizontal direction can be found in Figure 16. The measurement was performed three times in vertical as well as

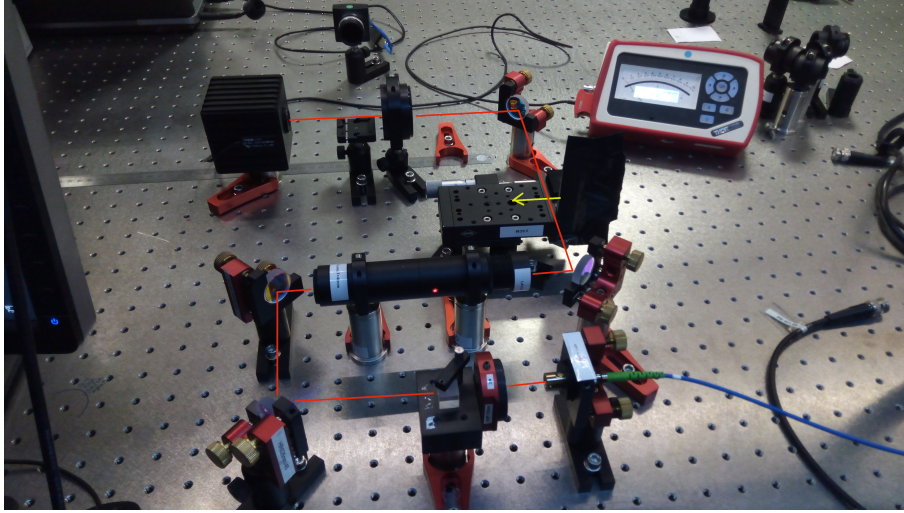


Figure 16: Experimental setup for the knife edge measurement in horizontal direction. The knife edge is mounted on a translation stage which is placed into the beam path. The position of the knife is varied using the micrometer of the stage. Thus, the power in the beam is measured at different knife positions after focussing the beam into the integrating sphere using a focussing lens.

in horizontal direction. The obtained data was fitted using the function given in Equation 26. A plot of the averaged data points in horizontal and vertical direction, respectively, can be found in Figure 17. To estimate the beam radius, the mean value of the fitted $w_{x/y}$ was calculated. This yields in horizontal direction a radius of

$$w_x = (3.30 \pm 0.02) \text{ mm}, \quad (40)$$

and in vertical direction

$$w_y = (2.98 \pm 0.02) \text{ mm}. \quad (41)$$

These radii are used to generate the input amplitude pattern. From the measurements, it is evident that the beam is elliptic. Meaning, the x and y radii are not equal. Therefore, the normalized intensity can be described by

$$I(x, y) = e^{-\frac{2x^2}{w_x^2}} e^{-\frac{2y^2}{w_y^2}}. \quad (42)$$

Taking the square root of the intensity yields the amplitude pattern.

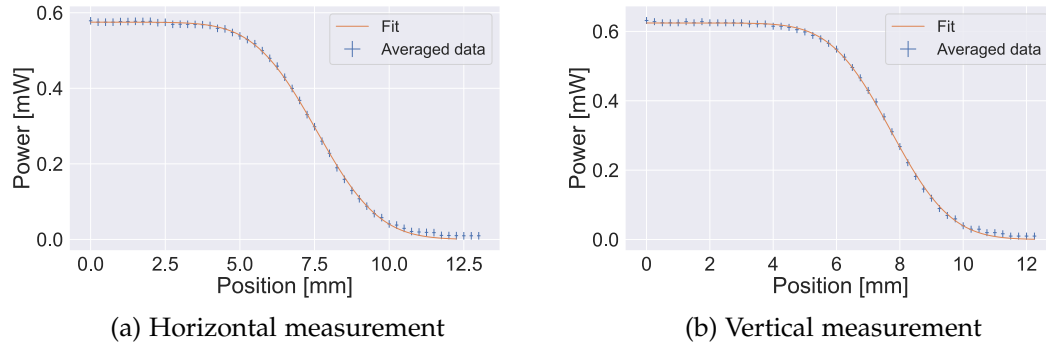


Figure 17: Plots of the fitted data after averaging over the 3 repetitions of the knife edge measurement to determine the dimensions of the beam incident on the SLM screen.

6.3. Diffraction efficiency of the Gratings

In order to spatially separate the outgoing beam from the incident beam and to separate the modulated beam from the unmodulated components, a grating was added to the final phase pattern given by our algorithm. The pattern of the grating was generated using the *Hamamatsu* software as discussed in Section 4.2.

Since it is desired to have as much intensity as possible in the desired diffraction orders (usually $+1$ or -1), the diffraction efficiency for different grating numbers, corresponding to the number of steps which approximate the sawtooth profile, was determined. In this measurement, only the grating and the correction pattern have been displayed on the screen of the SLM. We measured the power in the brightest diffraction order and compared it with the power in the incident beam to calculate the diffraction efficiency. By taking the ratio of these two values, the efficiency of the grating with different step sizes is obtained. The result is plotted in Figure 18. The numbers denoted at the data points ($+1$ or -1) describe the diffraction order we measured. As we can see in Figure 18, the diffraction efficiency increases by increasing the grating number. However, the distances between the diffraction orders decreases when increasing the grating number which can be seen in Figure 19. For this reason, a grating number of $n = 4$, where the diffraction orders are still distinguishable after a realistic propagation distance is used when evaluating the performance of the algorithm.

At a grating number of $n = 2$, the diffraction orders have the highest separation between them. Here, the diffraction efficiency of the first order is $33 \pm 4\%$. Using 4 grating steps, an efficiency of $50 \pm 3\%$ is obtained in the -1^{st} . In order to evaluate the effect of the diffraction efficiency of these two grating settings on the performance of our algorithm, we generate LG modes of azimuthal order $l = 1$ to $l = 8$ using our algorithm and add a grating to the respective phase patterns before displaying them on the SLM screen. We observe the output beam using a beam profiling camera. The

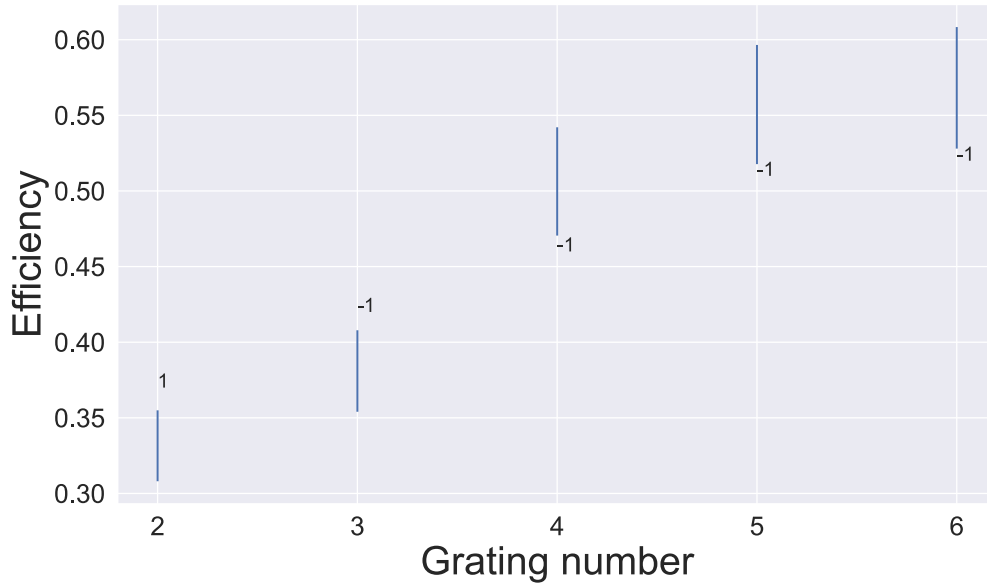


Figure 18: Graphical representation of the obtained data. The efficiency was calculated by dividing the power of the brightest diffraction order by the power of the incident beam. The order of diffraction measured is denoted at the data points.

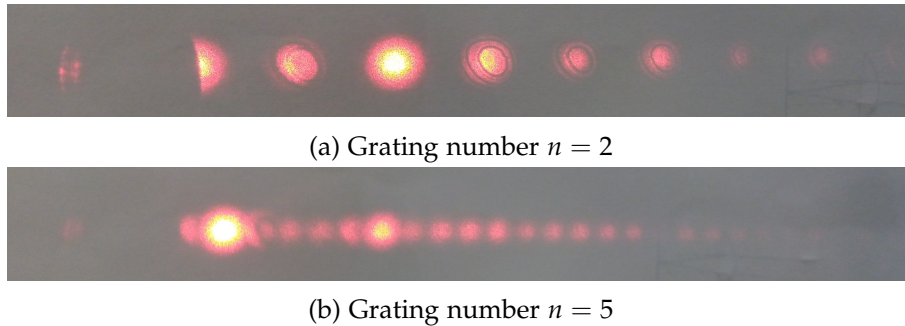


Figure 19: Picture of the diffraction orders of the grating with (a) 2 steps and (b) 5 steps. By increasing the grating number, the distances between the individual orders decreases and the orders overlap.

measurement is done for grating numbers 2 and 4. The observations can be found in Figure 20. The difference in the efficiencies becomes obvious in the brightness of the modes. All modes with a grating number of $n = 4$ are brighter than the corresponding mode with a grating number of $n = 2$.

In order to determine the light utilization efficiency of the implemented algorithm, we measured the power in the modulated LG modes using both grating numbers, $n = 2$ and $n = 4$, respectively, and divided this power by the power of the incident beam. The results are plotted in Figure 21. As expected, the efficiency when using a grating with 4

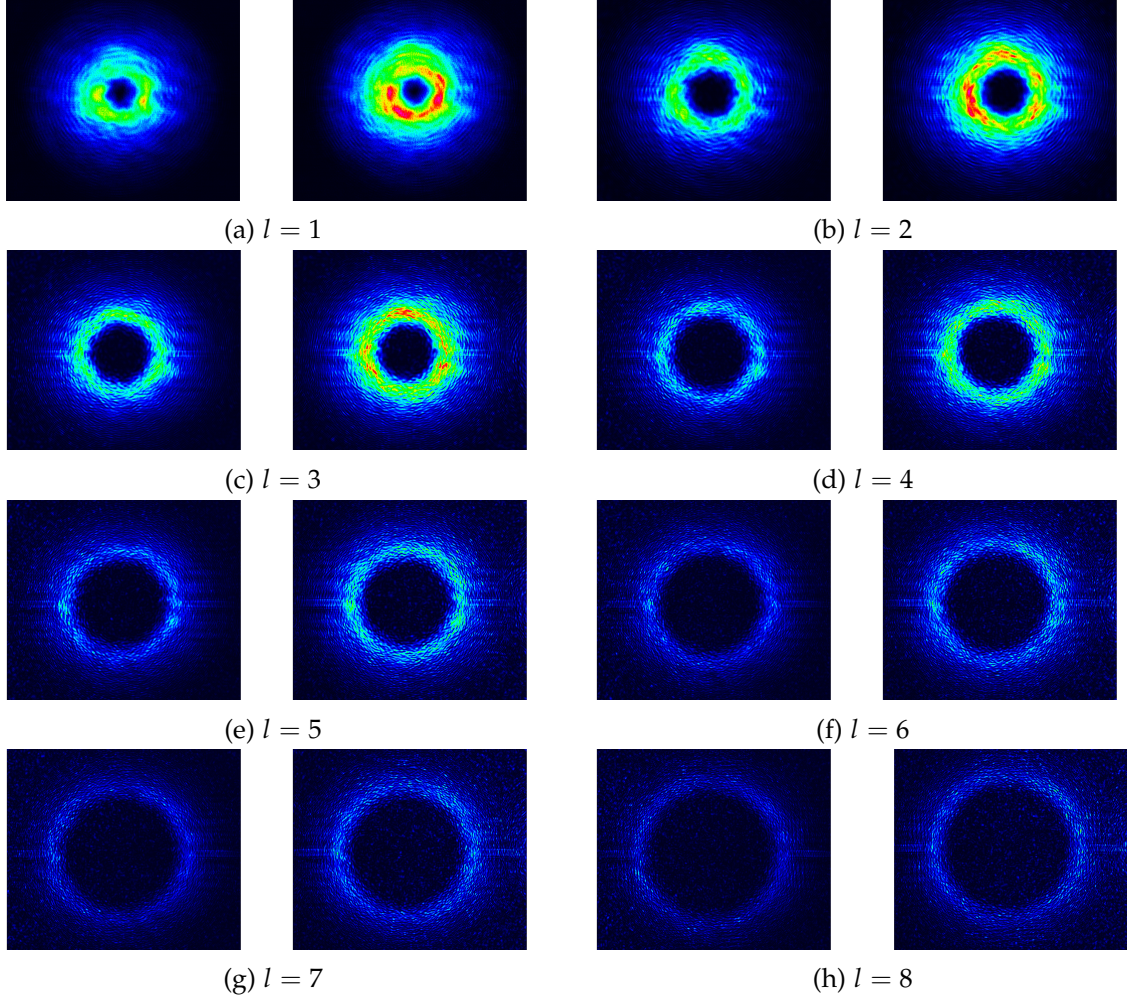


Figure 20: Pictures from the LG modes of different azimuthal orders l captured with the beam profiling camera. On the left of each subfigure, a grating with grating number $n = 2$ was used whereas on the right, the grating number is $n = 4$.

steps is larger than the efficiency when we use a grating with 2 steps. As we have already seen in the brightness of the captured modes, the light utilization efficiency decreases when increasing the order of the LG mode. For $l = 1$, the efficiency is $(40.8 \pm 2.8) \%$ for a grating number of $n = 4$ and $(28.9 \pm 2.0) \%$ for $n = 2$. It drops to $(11.4 \pm 0.8) \%$ and $(9.1 \pm 0.6) \%$ for $n = 4$ and $n = 2$, respectively, in the order $l = 8$.

6.4. Examination of the Purity of the Modes

In this section, the LG modes created by the *Hamamatsu* software and the algorithm are observed and compared. First, optical comparison is shown in Figure 22. As we can see, the inner radius of the LG beam is much larger when using the phase and amplitude shaping algorithm than the LG beams created by using the *Hamamatsu* software. Moreover, we observe some optical noise in the background when we use the

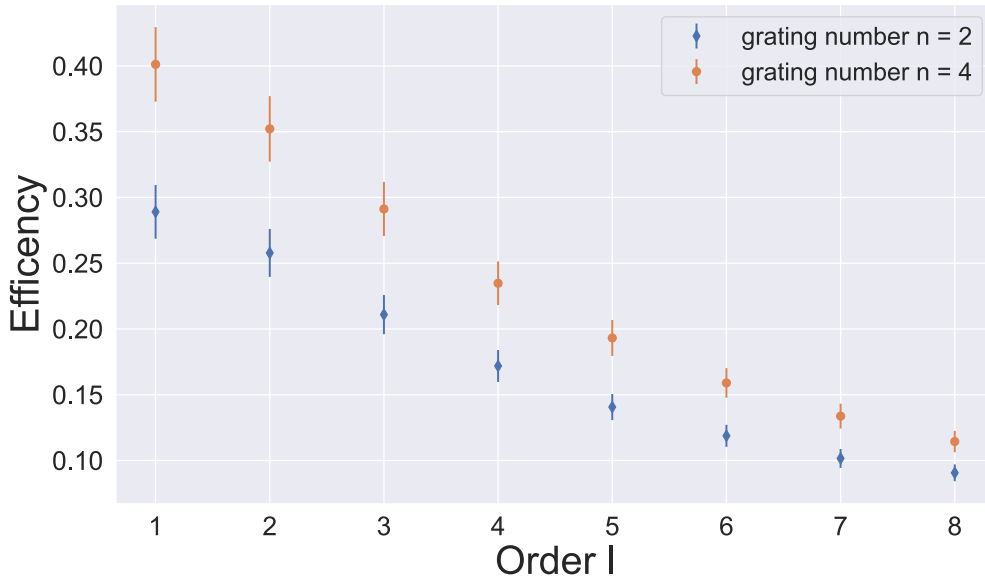


Figure 21: Light utilisation efficiency of the modes created with the holograms from the implemented algorithm. The efficiency decreases when increasing the azimuthal order l for both grating numbers, $n = 2$ and $n = 4$, respectively.

implemented algorithm. This can be explained by understanding the working of the algorithm: The final phase pattern at the end of each iteration is calculated by back propagating the complex wave field of the target beam and the propagated Gaussian beam modulated by some phase shift and then superimposing them. We have mentioned earlier that the initial phase shift is a random phase pattern. Since the desired LG mode vanishes in the center as well as on the edges on the calculated bitmap, the (nearly) only contribution to the final phase pattern at these positions is primarily defined by the random phase of the complex field of the propagated Gaussian beam after the first iteration.

In order to measure the purity of the LG modes, we used a beam profiling camera to measure the intensity line profiles of the output beams in the x - and y - directions. We implement both the methods at our disposal to compare and contrast them, 1) using the proprietary software from *Hamamatsu* and 2) using the implemented algorithm. The captured images for part 1) can be found in the appendix, Section B.1. Again, LG beams of azimuthal order $l = 1$ to $l = 8$ are considered.

The line profiles passing through the central singularity of the measured LG modes are directly measured by the beam profiling camera. The data measured along x - and y -

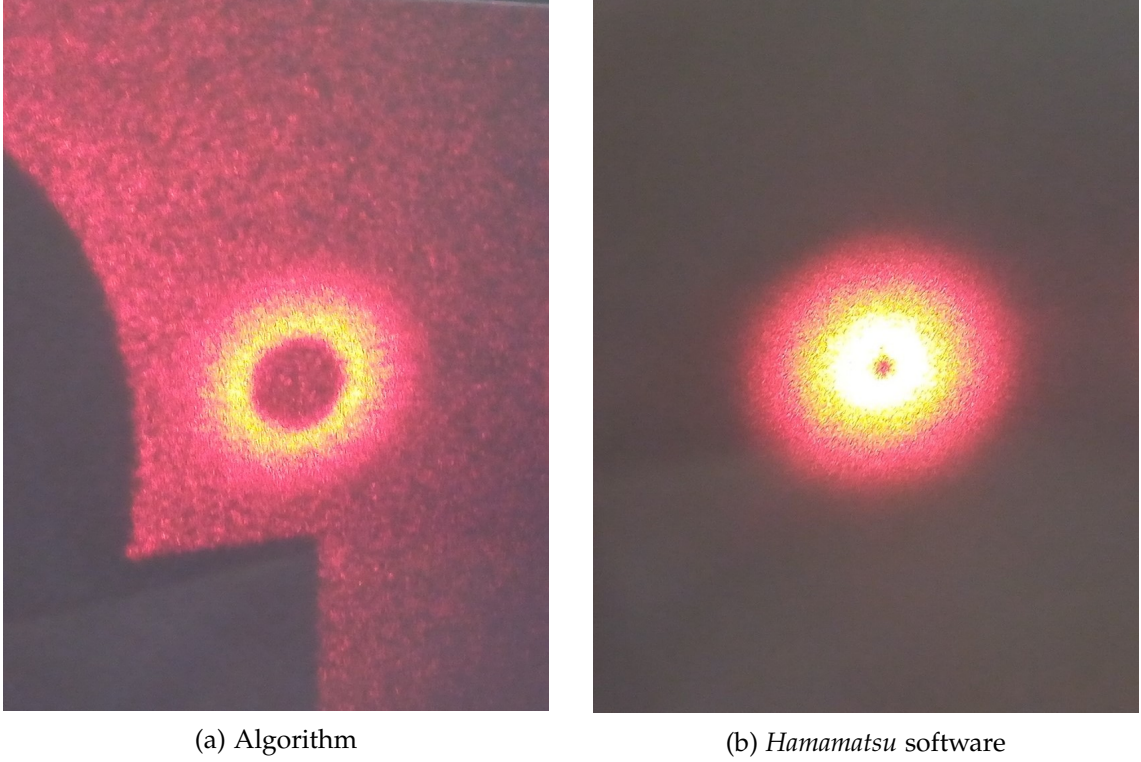


Figure 22: Pictures of the obtained LG beam with $l = 5$. The bitmap displayed on the SLM was calculated with (a) the implemented algorithm and (b) the proprietary software.

axis, respectively, are then fitted using

$$I_p^l(x) = B + C \frac{2}{\pi w_z^2} \frac{p!}{(p+l)!} \left(2 \frac{(x-a)^2}{w_z^2} \right)^l e^{\left(-2 \frac{(x-a)^2}{w_z^2} \right)} \left(L_p^l \left(2 \frac{(x-a)^2}{w_z^2} \right) \right)^2, \quad (43)$$

which is known from [16]. While the radial order p and the azimuthal order l are fixed, the intensity offset B , scaling factor C , position offset a and beam waist of the ring w_z are fit parameters, respectively.

Moreover, we will perform the measurements for two gratings with grating number $n = 2$ and $n = 4$, respectively to examine if the purity of the mode is influenced by the grating. The fits for a grating number of 4 using the implemented algorithm in x - and y -direction are shown in Figures 29 and 30, respectively. Figures 31 and 32 illustrate the fits of the line profiles of the LG modes with a grating number of $n = 4$ that were created by the *Hamamatsu* software in x - and y -direction, respectively. All fits with $n = 2$ can be found in the appendix, Section B.2.

As a measure for the purity, we will use the beam waist w_z of the modes as well as the inner and outer radii of the circular amplitude pattern of the modes. Note that we do not use some kind of a goodness of fit measure to estimate mode purity since it does

not accurately determine how closely our generated mode resembles the ideal intensity profile: Even when a function fits very well to the data, the intensity profile of the LG mode could deviate significantly from what is to be expected theoretically, for the given experimental parameters. An example for this is the beam waist w_z . In order to find a correct fit to our data, w_z has to be a fit parameter. However, since we do not change the dimensions of the incident beam over the course of this measurement, it should stay stable for all data points, or in this case, all orders of the LG modes. If we only evaluate the goodness of the fit, we would not take into account the stability of this value. As another measure for purity, we will also use the inner and outer radii of the beam since it does depend on the order l and the beam waist and should increase with l .

When we create the LG beams with the algorithm, these values will also be compared to the values for beam waist and radii of the target amplitude profile. The line profiles of the target amplitude are also illustrated in the appendix, Section B.2.

6.4.1. Beam waist of the Modes

Since the beam waist w_z should stay constant for all modes, the stability of this value by increasing the azimuthal order l of the LG mode is observed.

If the beam is modulated using the *Hamamatsu* software, the beam waist decreases with increasing the azimuthal order of the LG beam. The values are shown in Table 1. This behaviour is observed for both x - and y -direction and is plotted in Figure 23. In x -direction, the difference between the maximum fitted beam waist and the minimal value for w_z is $(55 \pm 0.3) \%$ whereas the difference in y -direction is even higher at $(60 \pm 0.3) \%$. Hence, the mode purity is considerably low when using the phase holograms that can only modulate phase.

When we use the holograms that are calculated by the implemented algorithm, the

Order l	w_z^x [μm]	w_z^y [μm]	Order l	w_z^x [μm]	w_z^y [μm]
1	1389.8 ± 8.3	1430.8 ± 9.4	1	1413.5 ± 8.2	1510.8 ± 8.1
2	1038.1 ± 5.9	1121.4 ± 6.6	2	987.7 ± 5.4	1138.9 ± 6.4
3	850.1 ± 4.2	789.0 ± 3.9	3	840.4 ± 3.8	800.5 ± 4.2
4	751.1 ± 3.2	711.7 ± 3.2	4	753.3 ± 3.0	707.6 ± 3.2
5	707.7 ± 2.7	659.5 ± 2.6	5	703.0 ± 2.6	665.5 ± 2.7
6	678.5 ± 2.4	644.5 ± 2.3	6	673.5 ± 2.3	644.4 ± 2.3
7	650.5 ± 2.1	621.0 ± 2.0	7	651.2 ± 2.1	628.1 ± 2.0
8	636.6 ± 1.9	620.2 ± 1.9	8	637.4 ± 1.9	616.9 ± 1.9

(a) Grating number $n = 2$

(b) Grating number $n = 4$

Table 1: The beam waists in x - and y -direction, w_z^x and w_z^y , respectively. The LG modes are created with the *Hamamatsu* software.

beam waist w_z stays more stable along both axes. In Figure 24, it is plotted against the

azimuthal order l of the LG beam. Along x , there is a difference in the beam waist of $(15.0 \pm 0.6)\%$ between the lowest and the highest value whereas the fluctuations in y -direction are $(13.4 \pm 0.6)\%$.

According to Reference [27], it should be possible to obtain arbitrary beam shapes

Order l	w_z^x [μm]	w_z^y [μm]	Order l	w_z^x [μm]	w_z^y [μm]
1	1740.3 ± 7.4	1742.7 ± 6.6	1	1626.2 ± 7.4	1757.0 ± 5.6
2	1688.2 ± 5.9	1608.7 ± 4.8	2	1638.1 ± 5.5	1608.9 ± 4.7
3	1765.8 ± 5.2	1594.5 ± 5.8	3	1687.7 ± 5.1	1577.0 ± 5.0
4	1790.0 ± 5.3	1623.9 ± 4.9	4	1735.3 ± 6.0	1618.2 ± 5.8
5	1830.2 ± 6.0	1661.1 ± 6.6	5	1775.9 ± 6.9	1655.2 ± 6.5
6	1819.3 ± 7.1	1683.9 ± 6.7	6	1823.2 ± 8.3	1696.5 ± 6.6
7	1871.4 ± 7.3	1754.9 ± 8.7	7	1855.2 ± 8.9	1754.9 ± 8.0
8	1913.6 ± 7.5	1762.6 ± 10.2	8	1866.9 ± 9.1	1820.0 ± 9.7

(a) Grating number $n = 2$ (b) Grating number $n = 4$

Table 2: The beam waists in x - and y - direction, w_z^x and w_z^y , respectively. The LG modes are created with the implemented algorithm.

with this algorithm. Thus, we expect that the beam waist of the observed LG mode corresponds to the beam waist of the LG mode in our target amplitude pattern. In order to test this expectation, w_z of the target pattern is compared to the weighted mean values of w_z obtained from the line profiles in x - and y - direction for LG beams with azimuthal order $l = 1$ through $l = 8$.

The line profiles of the target patterns are obtained by plotting a row and a column of the matrix representing the target amplitude against the x - and y - dimensions, respectively. Equation 43 is then fitted to these data. As expected, the beam waist does not vary with l and is the same along both axes. It results in

$$w_z^{\text{target}} = 2402.6 \mu\text{m}. \quad (44)$$

This value is larger than the weighted mean values of the beam waist of the observed beam. In x - direction, it is given by

$$\bar{w}_z^x = (1702.5 \pm 1.6) \mu\text{m}, \quad (45)$$

and in y -direction, it is

$$\bar{w}_z^y = (1612.5 \pm 1.5) \mu\text{m}. \quad (46)$$

Hence, the deviation between the target beam waist and the measured beam waist along the x -axis is $(29.14 \pm 0.04)\%$ and in y - direction, it is $(32.88 \pm 0.06)\%$.

In order to find the source of this unexpected difference, the radii of the incident Gaussian beam were checked once again using the beam profiling camera. This delivered in x -direction a waist of $w_x = (3100 \pm 15) \mu\text{m}$ and $w_y = (2800 \pm 16) \mu\text{m}$ in

y -direction. The holograms created by the algorithm were calculated with these dimensions once again and the measurement of the LG modes was repeated. Nevertheless, the measured beam waist results in $\bar{w}_z^x = (1706.1 \pm 1.6) \mu\text{m}$ and $\bar{w}_z^y = (1611.2 \pm 1.4) \mu\text{m}$ which is almost the same as the measurements with the beam waists obtained using the knife edge measurement.

6.4.2. Inner and Outer radii of the LG modes

Another possibility to evaluate the obtained modes is to measure the inner and outer radii, r_1 and r_2 , respectively, of the intensity profiles of the LG modes. We therefore use the fits from above and calculate their $1/e^2$ width.

Since we expect the inner and outer radii of our measured LG modes to be the same as the corresponding inner and outer radii values of our target amplitude pattern, we compare the deviation between these 2 values to evaluate the purity of the modes. In Figure 25 and Figure 26, the measured values for the inner and outer radii are compared to the ones of the target pattern, respectively. We can see that the increase of the radii with respect to the azimuthal order of the measured modes follows a similar trend as seen in the target profiles. However, the measured radii are smaller than compared to the target radii. This is caused by the lower beam waists of the modulated modes compared to the beam waists of the target modes.

In contrast, the LG modes which are generated by the holograms from the *Hamamatsu* software do not fit to the expected values. Since we do not have target profiles when we create the holograms with this software, we use theoretical formulas for the inner and outer radii which are known from [18]. The radii are given by

$$r_1 = \frac{1}{\sqrt{2}} (l + 1.3 - \sqrt{q_l})^{\frac{1}{2}}, \quad (47)$$

and

$$r_2 = \frac{1}{\sqrt{2}} (l + 1.3 + \sqrt{q_l})^{\frac{1}{2}}, \quad (48)$$

respectively, with the order l of the vortex beam and the definition

$$q_l = (l + 1.3)^2 - l^2 e^{-\frac{14}{l}}. \quad (49)$$

The radii are defined in units of the beam waist w_0 of the Gaussian beam that is incident on the SLM. Hence, we multiply the above expressions by the beam waists w_x and w_y , to compare them to the radii of the observed beam widths in x - and y -direction, respectively. A graphical representation can be found in the Figures 27 and 28. It can be clearly seen that the observed outer radii does not follow the trend that we expect.

Similarly, for the inner radii, there is a marginal increase with the azimuthal order l . Nevertheless, the slope is very different from what we expect.

In Tables 3 to 6, all measurements for the radii are tabulated. When comparing measurements for the implemented algorithm, it is obvious that in x -direction, inner and outer radii are about 26 % smaller than the radii of the respective target beam. In y -direction, the radii are approximately 30 % smaller than the target radii. These deviations are close to the difference between the measured beam waists compared to the target beam waists as calculated in Section 6.4.1.

As we have already seen in the plots, there are clearly larger deviations from the theoretical radii to the measured radii when we use the phase-only modulating *Hamamatsu* software. Hence, this measurement brings out the motivation behind trying to achieve amplitude modulation using a phase-only SLM and also gives an idea about the performance of this algorithm,

order l	target r_2 [μm]	r_2^x [μm]	r_2^y [μm]
1	2607.13	2527.20	2627.20
2	4262.67	2950.88	2854.38
3	4778.40	3434.39	3153.97
4	5218.19	3828.39	3520.89
5	5608.27	4208.92	3870.68
6	5962.51	4519.93	4194.77
7	6289.30	4877.73	4594.12
8	6594.20	5188.28	4916.70

Table 3: Outer radii of the LG modes from the algorithm compared to the target radii. The denoted inner radii of the observed modes are the mean value of the radii we measured with a grating number $n = 2$ and $n = 4$, respectively.

order l	target r_1 [μm]	r_1^x [μm]	r_1^y [μm]
1	388.62	303.46	283.05
2	956.06	568.90	640.20
3	1441.14	1035.80	951.22
4	1865.44	1368.60	1258.67
5	2246.17	1685.72	1550.25
6	2594.16	1966.52	1825.05
7	2916.48	2261.91	2130.39
8	3218.03	2531.92	2399.39

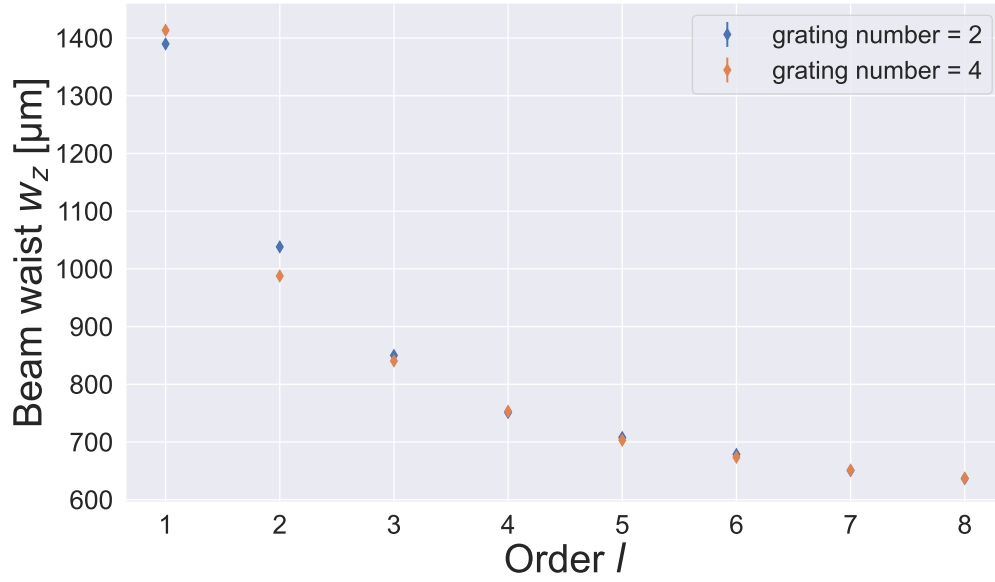
Table 4: Inner radii of the LG modes from the algorithm compared to the target radii. The denoted outer radii of the observed modes are the mean value of the radii we measured with a grating number $n = 2$ and $n = 4$, respectively.

order l	Theoretical r_2^x [μm]	Theoretical r_2^y [μm]	r_2^x [μm]	r_2^y [μm]
1	4975.10	4492.67	2104.40	2208.23
2	5849.43	5282.21	1797.12	2005.20
3	6552.04	5916.69	1681.10	1580.74
4	7154.46	6460.70	1636.08	1541.43
5	7689.85	6944.17	1646.58	1546.53
6	8176.46	7383.59	1677.64	1599.39
7	8625.56	7789.14	1703.75	1634.98
8	9044.66	8167.61	1748.29	1697.77

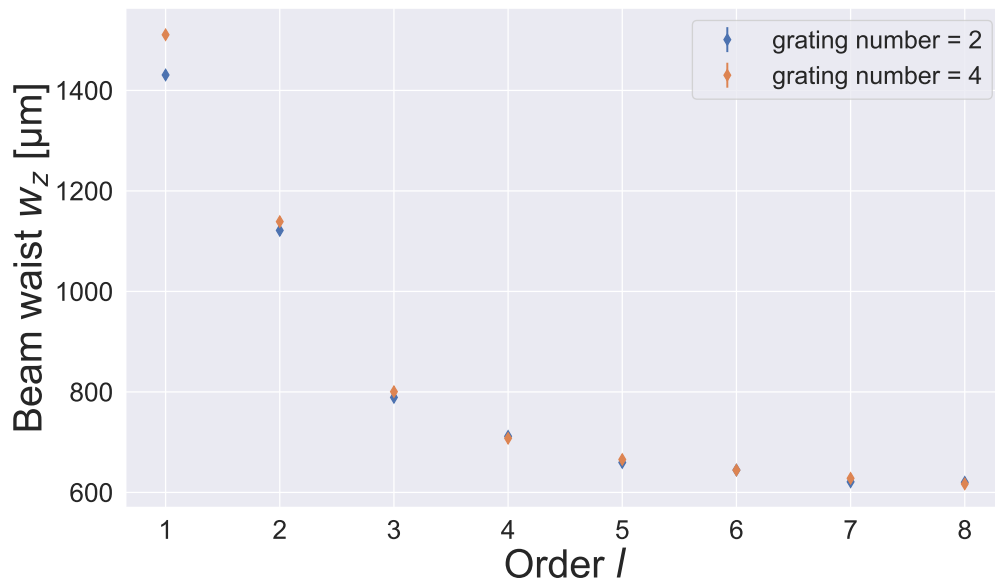
Table 5: Outer radii of the LG modes from the *Hamamatsu* software compared to the target radii in x - and y - direction, respectively. All measured radii are mean values of the results for a grating number of $n = 2$ and $n = 4$.

order l	Theoretical r_1^x [μm]	Theoretical r_1^y [μm]	r_1^x [μm]	r_1^y [μm]
1	543.49	490.79	112.44	237.91
2	1311.93	1184.71	389.67	449.74
3	1974.27	1782.83	457.85	476.74
4	2555.52	2307.71	503.43	551.04
5	3077.86	2779.40	659.47	619.40
6	3555.63	3210.84	729.91	695.86
7	3998.33	3610.62	790.01	756.91
8	4412.60	3984.71	853.18	828.52

Table 6: Inner radii of the LG modes from the *Hamamatsu* software compared to the target radii in x - and y - direction, respectively. All measured radii are mean values of the results for a grating number of $n = 2$ and $n = 4$.



(a) x -direction



(b) y -direction

Figure 23: Plots of the beam waist w_z in x - and y -direction for several LG modes. The modes are generated by using the holograms which are calculated by the *Hamamatsu* software. Contrary to our expectations, w_z does not stay constant.

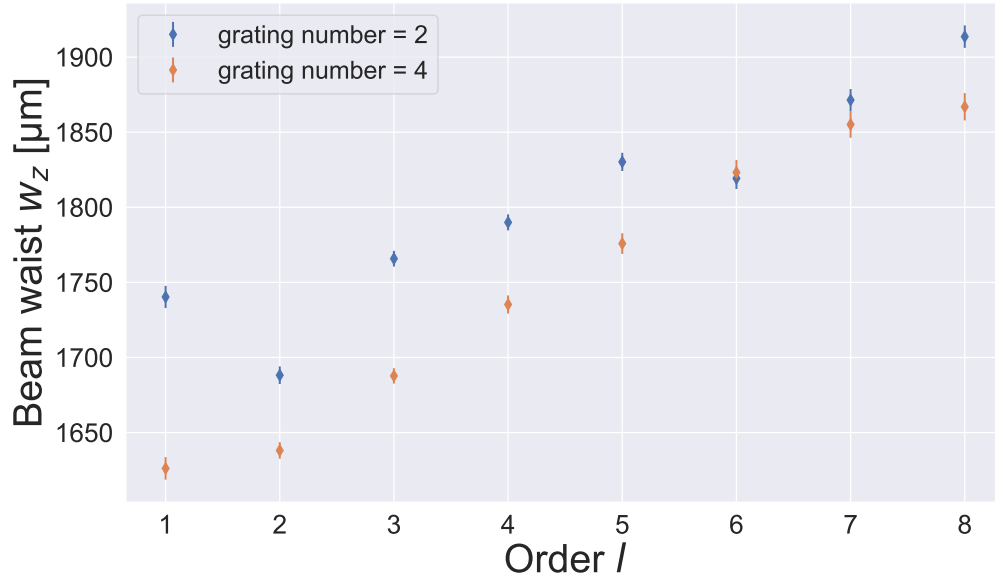
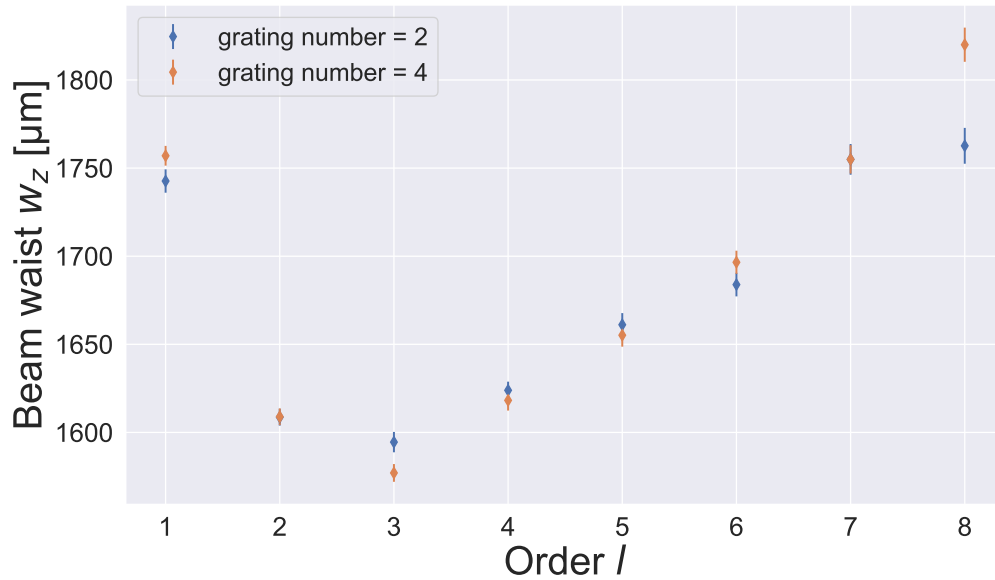
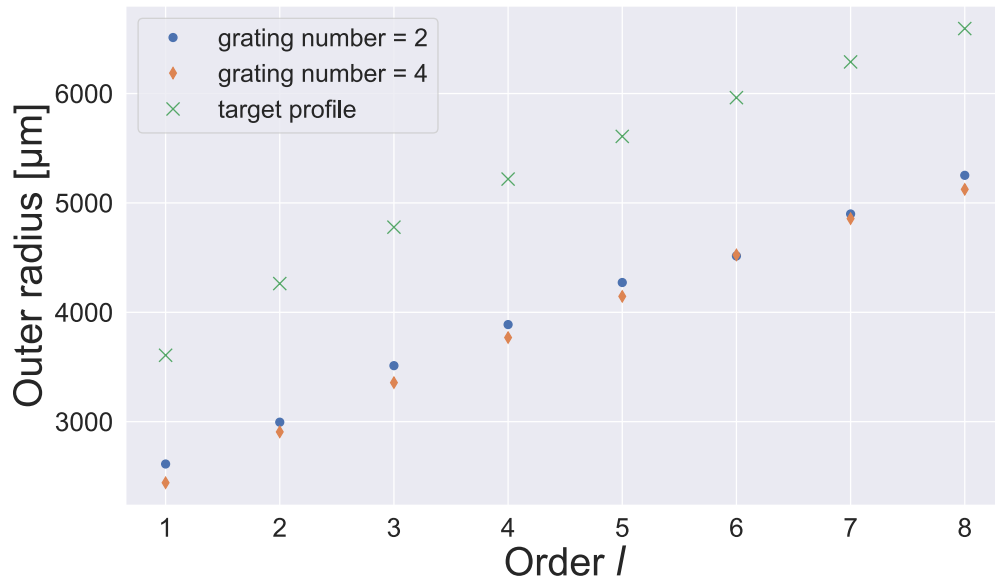
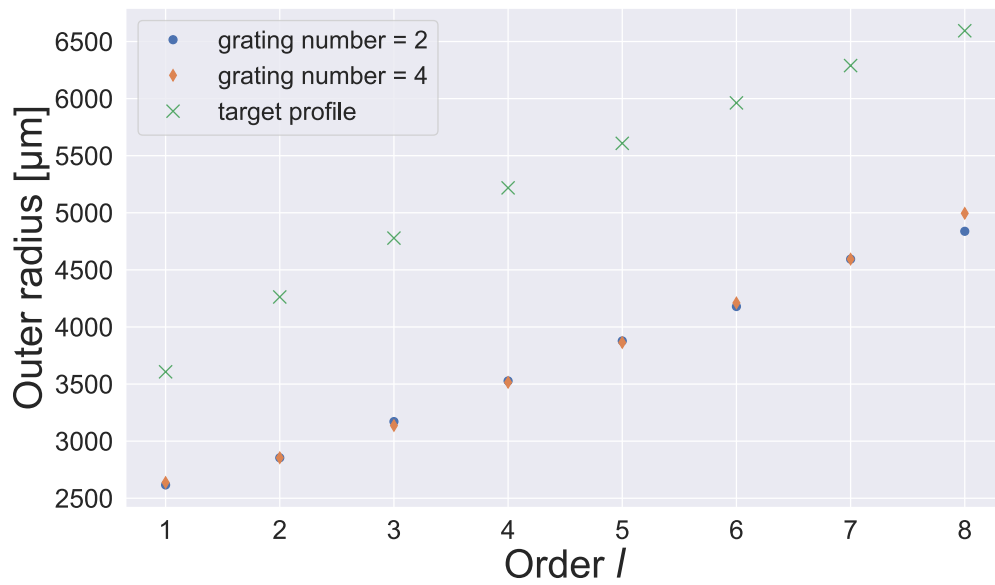
(a) x -direction(b) y -direction

Figure 24: Plots of the beam waist w_z in x - and y -direction for several LG modes. The holograms to obtain these modes are calculated by the implemented algorithm. The fluctuations of w_z are lower than for the LG beams which are created by the *Hamamatsu* software.

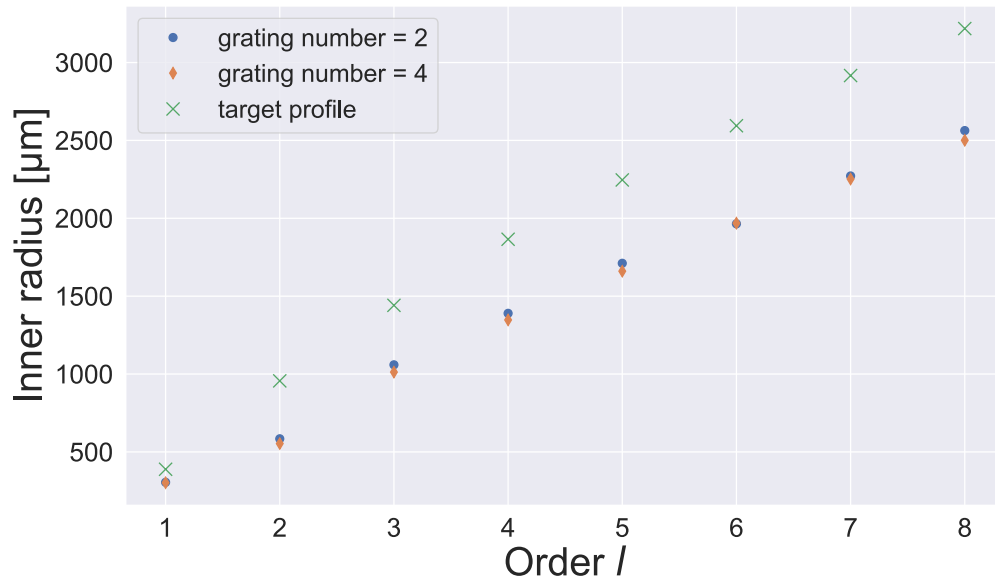


(a) x -direction

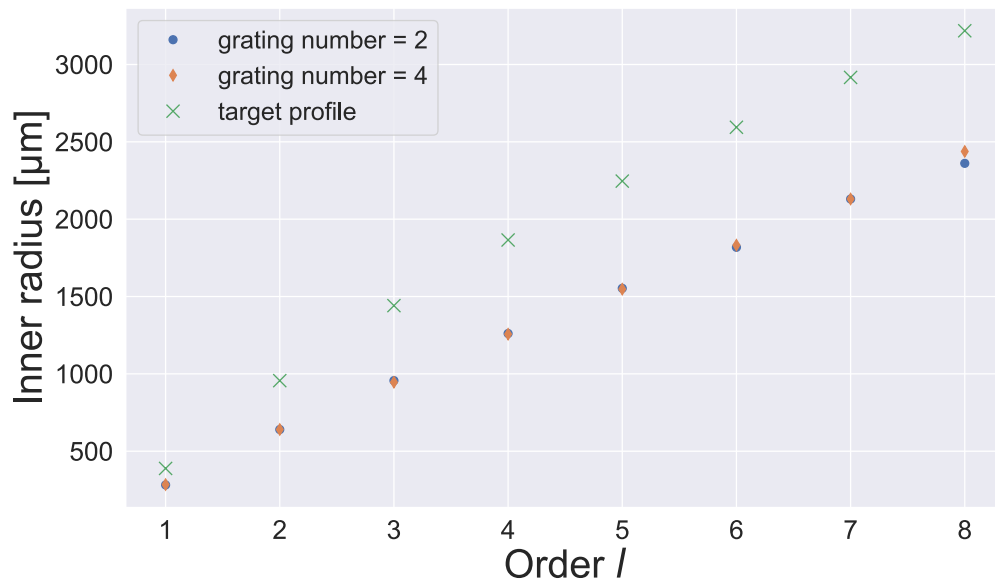


(b) y -direction

Figure 25: Plots of the outer radius in x - and y - direction, respectively, when using the implemented algorithm.

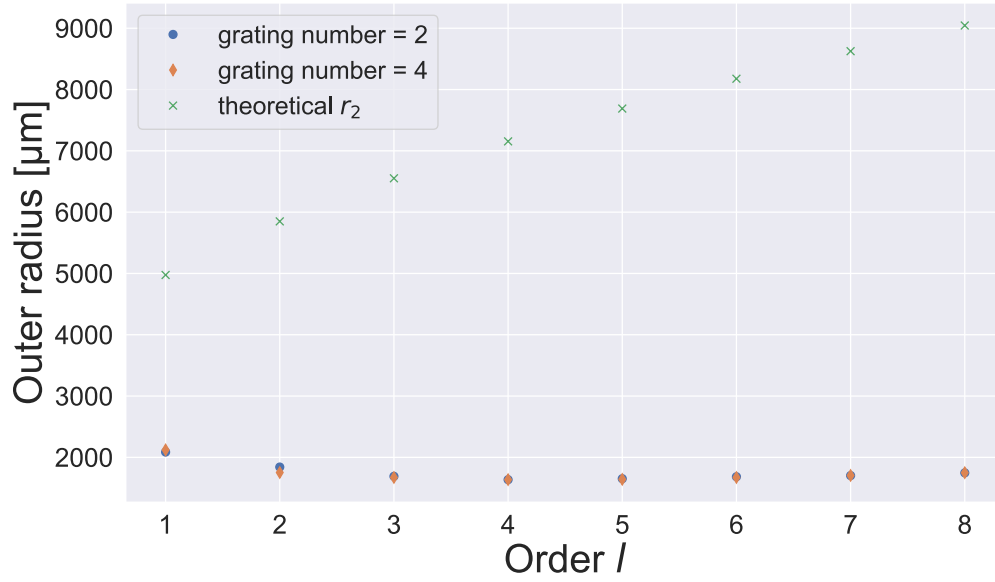


(a) x -direction

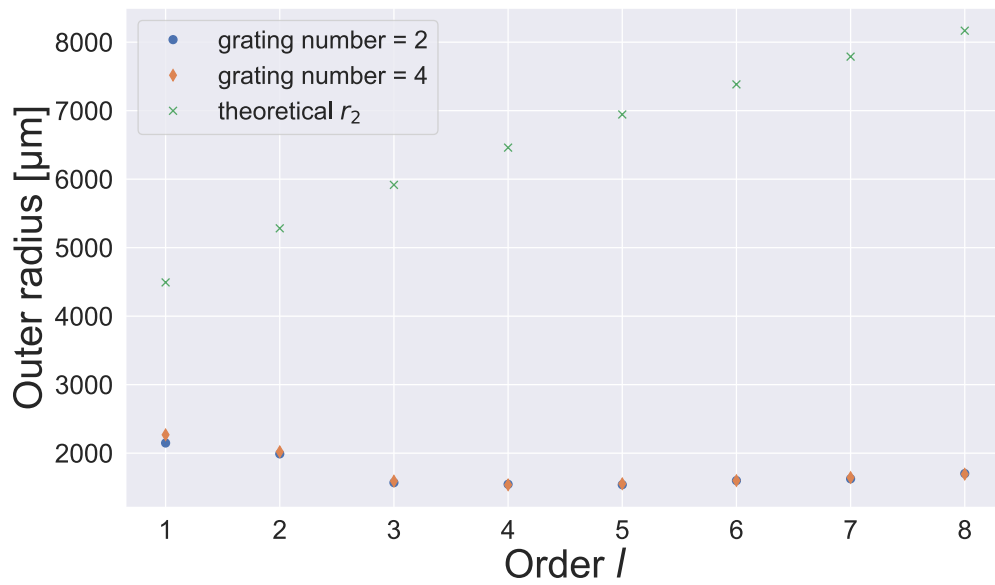


(b) y -direction

Figure 26: Plots of the inner radius in x - and y - direction, respectively, when using the implemented algorithm.

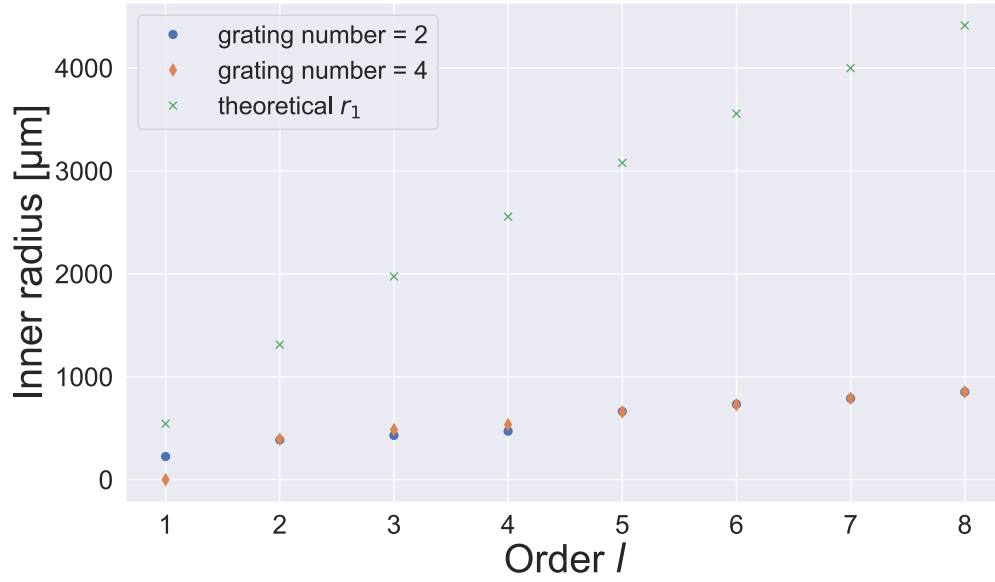


(a) x -direction

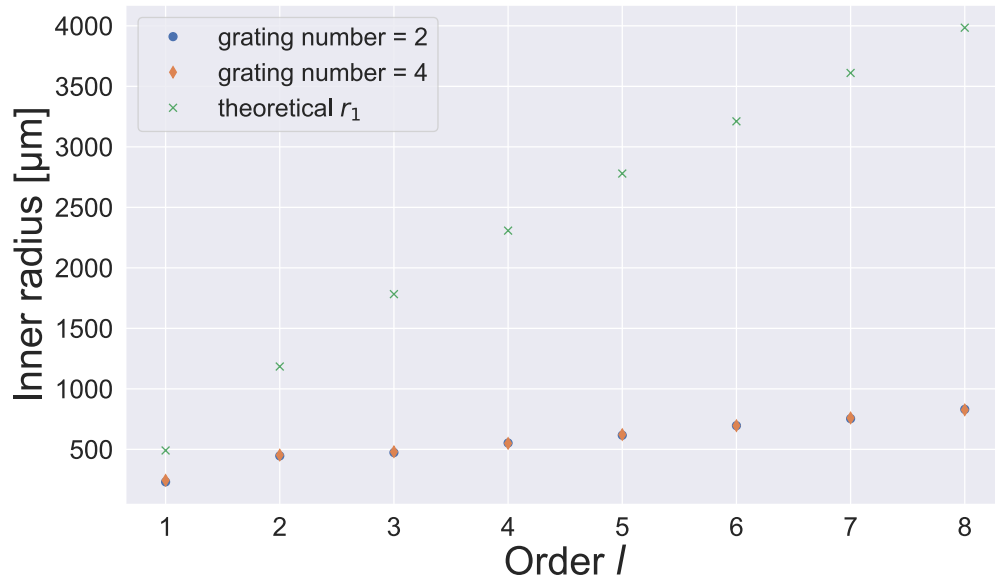


(b) y -direction

Figure 27: Plots of the outer radius in x - and y - direction, respectively, when using the software of the manufacturer. The radii of the modulated LG modes are smaller than according to the theoretical formulas.



(a) x -direction



(b) y -direction

Figure 28: Plots of the inner radius in x - and y - direction, respectively, when using the software of the manufacturer. The radii of the modulated LG modes are smaller than according to the theoretical formulas.

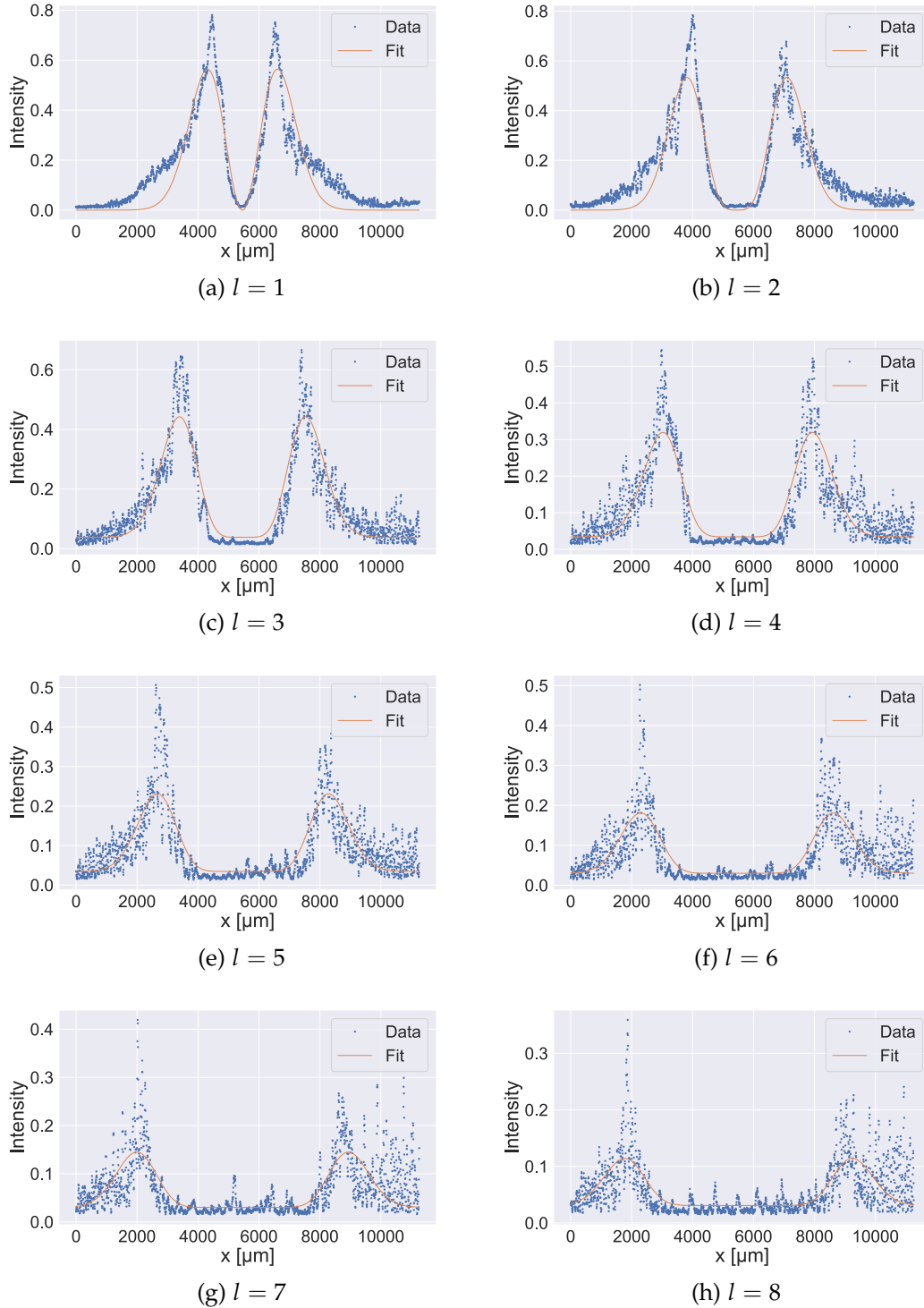


Figure 29: Plots of the line profiles of the LG modes with different azimuthal orders in x -direction. The holograms were calculated with the implemented algorithm and were combined with a blazed grating of $n = 4$.

6.4 Examination of the Purity of the Modes

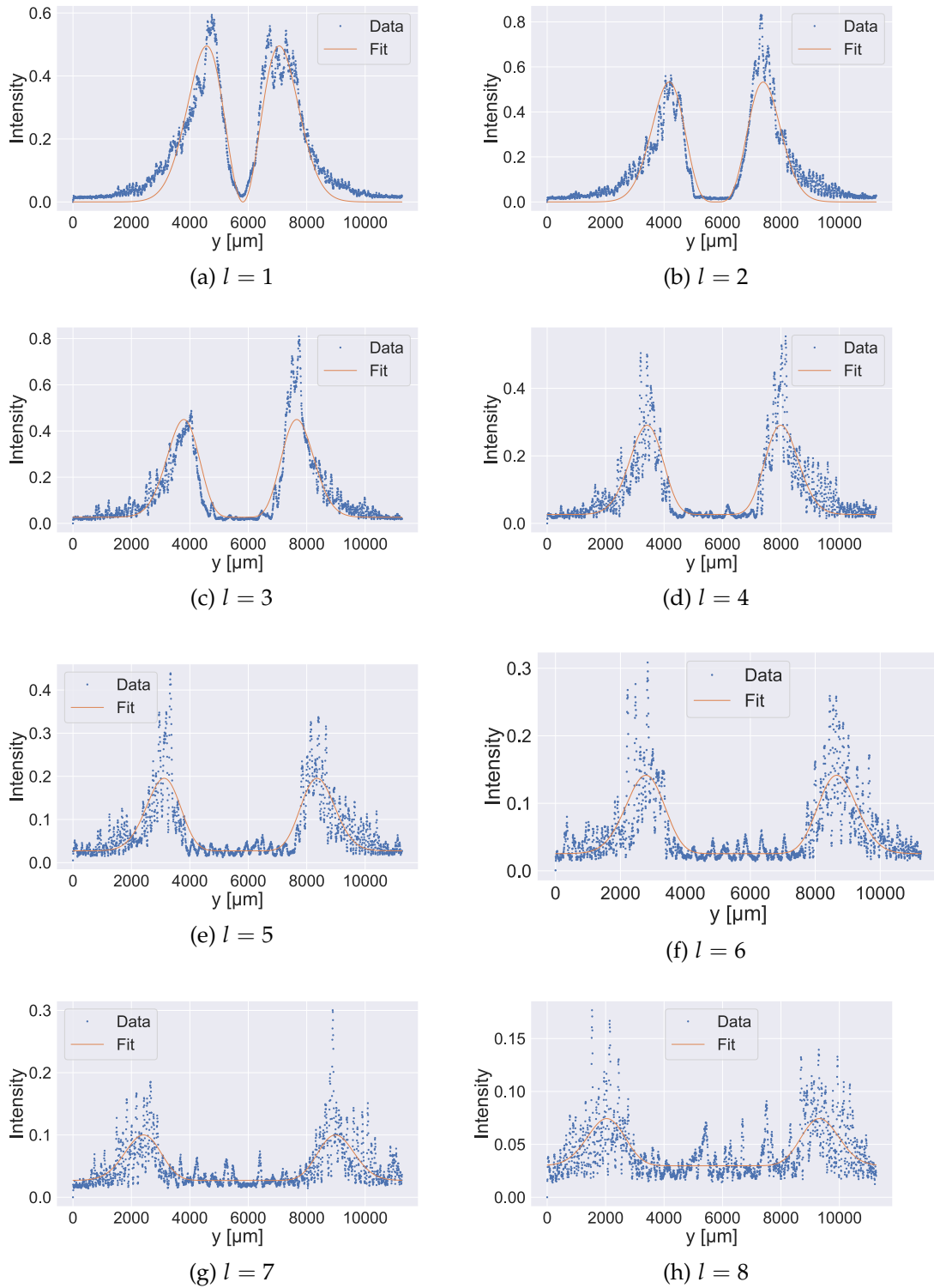


Figure 30: Plots of the line profiles of the LG modes with different azimuthal orders in y -direction. The holograms were calculated with the implemented algorithm and were combined with a blazed grating of $n = 4$.

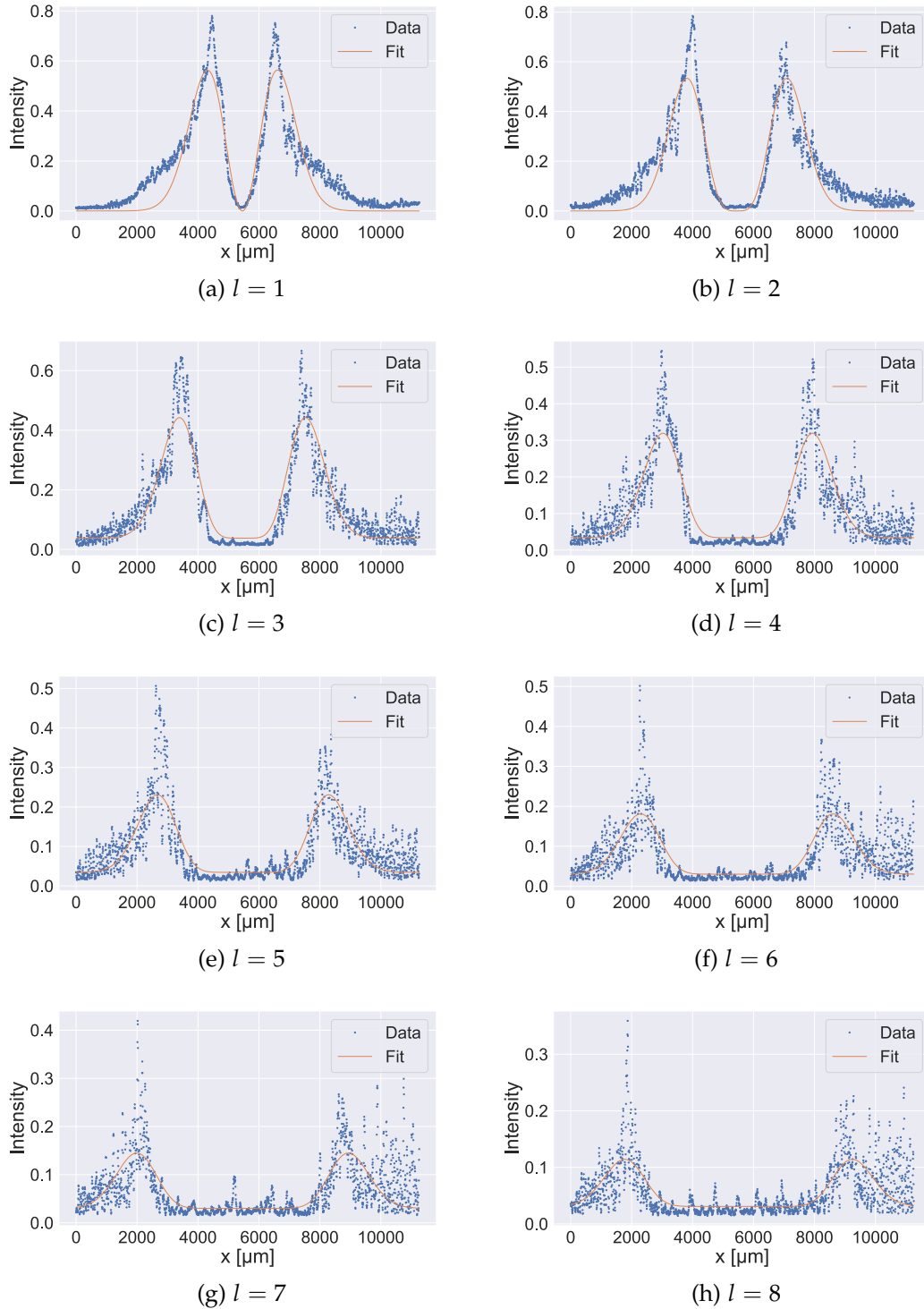


Figure 31: Plots of the line profiles of the LG modes with different azimuthal orders in x -direction. The modes are generated by using the holograms which are calculated by the *Hamamatsu* software. A blazed phase grating with grating number $n = 4$ is added to the final phase pattern.

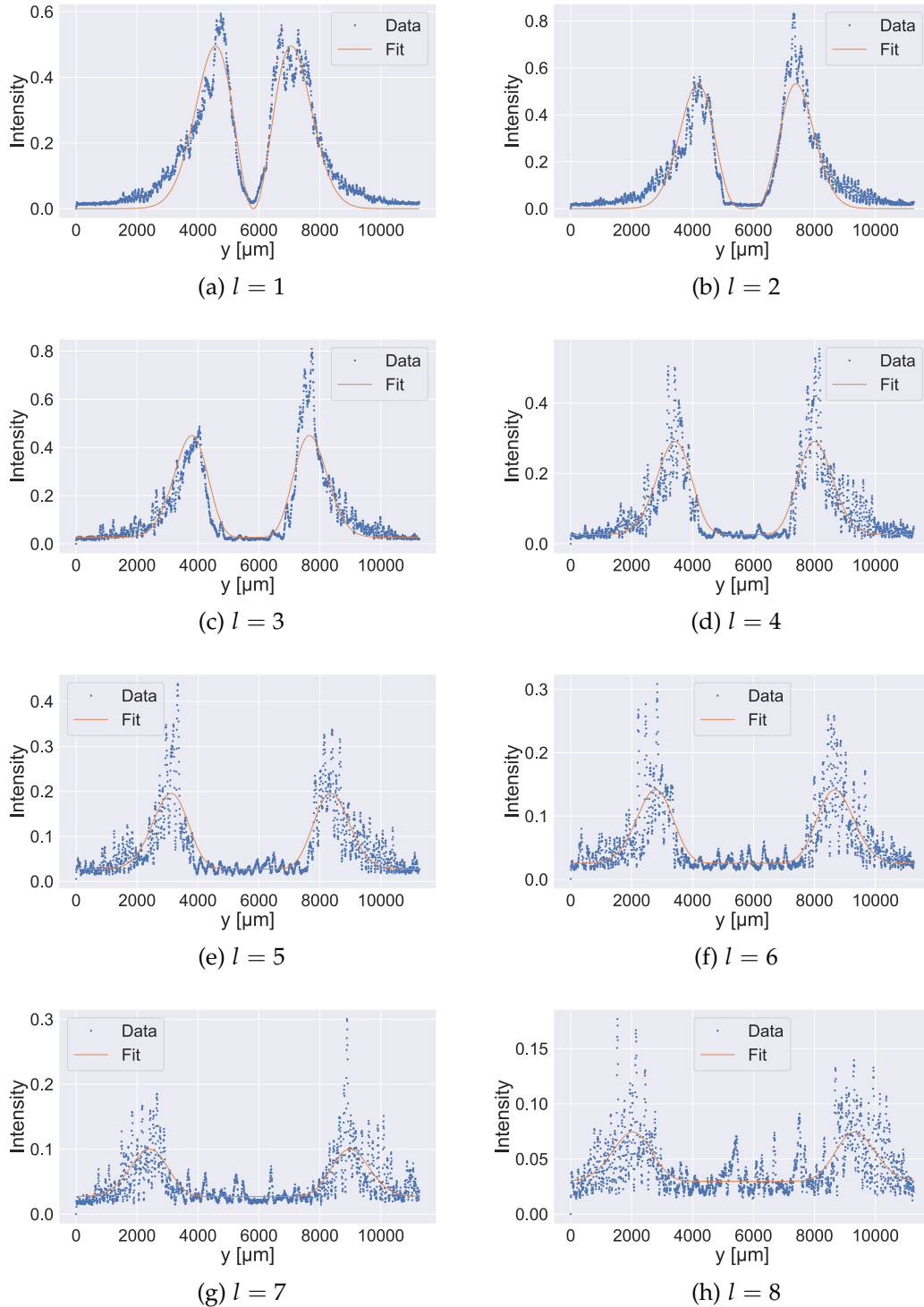


Figure 32: Plots of the line profiles of the LG modes with different azimuthal orders in y -direction. The modes are generated by using the holograms which are calculated by the *Hamamatsu* software. A blazed phase grating with grating number $n = 4$ is added to the final phase pattern.

7. Conclusion and Outlook

In the context of this work, we could generate LG modes using a phase-only LCOS-SLM. The holograms that were displayed on the SLM were calculated by the proprietary software provided by the manufacturer and also by an implemented algorithm from [27]. The advantage of the algorithm is that it enables us to generate a phase-only hologram which could simultaneously modulate both, the amplitude and phase of a complex wave field. With the control of both, phase and amplitude, we expected a higher purity of the optical modes we generated. In order to quantify the purity, we measured the beam waist as well as the inner and outer radii of the intensity patterns.

In the measurement of the beam waist, we looked at the stability of this value when fitting the data. The results were presented in Section 6.4.1. We see that when using the hologram created by the proprietary software, the beam waist decreases rapidly by increasing the azimuthal order of the LG modes. In contrast, when using the holograms generated by the algorithm, the fluctuations in beam waists of the modes are considerably reduced. However, the beam waist was about 33% smaller than the target amplitude profiles. The reason behind this observation needs to be investigated further. The evaluation of inner and outer radii, which was presented in Section 6.4.2, emphasized once again the utility of the algorithm. For the LG modes generated using the proprietary software, the radii did not follow the trend that they are expected to follow, as described in Reference [18]. On the other hand, when we used the holograms created by the implemented algorithm, we compared the radii of the measured LG modes to the radii of the amplitude profile of the target mode which we used while calculating the phase hologram. Here, all measured radii followed the trend of that was expected, albeit some offset. This is similar to what we also observed for the beam waist measurement.

For further measurements, we plan to analyze the propagation and divergence of the resulting LG beams to get an even better understanding of their properties. To investigate the offset issue with the beam waist and radii, as mentioned in the previous paragraph, we plan to take an image of the incident beam using our beam profiling camera, and then use this image as the incident field pattern while implementing the algorithm. One can expect that by doing so, we can take into account the small deviations from a perfect Gaussian intensity profile of the incident beam, and in the process, improve the purity of the generated optical mode.

As mentioned in the introduction, we also want to create OV beams by controlling the local polarisation of OAM beams. For that purpose, it would be necessary to implement another algorithm, which also requires a more elaborate experimental setup, e. g. as presented in [25].

A. Fitting methods and mathematics

A.1. Generalized Laguerre polynomials

According to [26], the generalized Laguerre polynomials are defined by a recursive function,

$$L_{n+1}^{(\alpha)}(x) = \frac{2n+1+\alpha-x}{n+1}L_n^{(\alpha)}(x) - \frac{n+\alpha}{n+1}L_{n-1}^{(\alpha)}(x), \quad (50)$$

for $n > 1$. The initial conditions are given by

$$L_0^{(\alpha)}(x) = 1, \quad L_1^{(\alpha)}(x) = 1 + \alpha - x. \quad (51)$$

A.2. Weighted Mean value

We calculate the weighted mean value \bar{A} of some data points A_i according to the definition

$$\bar{A} = \sum_i \frac{1}{w_i} \sum_i w_i A_i, \quad (52)$$

which is known from [7]. The weights w_i are defined as $w_i = \frac{1}{\sigma_i}$ where σ_i represents the error of each data point A_i

A.3. Fitting methods

In general, the presented fits were performed using the Python command `curve_fit` from the `scipy.optimize` package. It uses the least square method to fit the data with the specified fit function.

The only exceptions are the fits for the knife edge measurements. Here, we use the Python command `ODR` from the `scipy.odr` package. The reason for that is that it calculates the fit with the orthogonal distance regression which takes into account errors in x - and y -direction. Since the measurement of power, as well as the position of the knife edge contains some errors, this method is more suitable.

B. Additional Figures

B.1. Pictures from the beam profiling camera

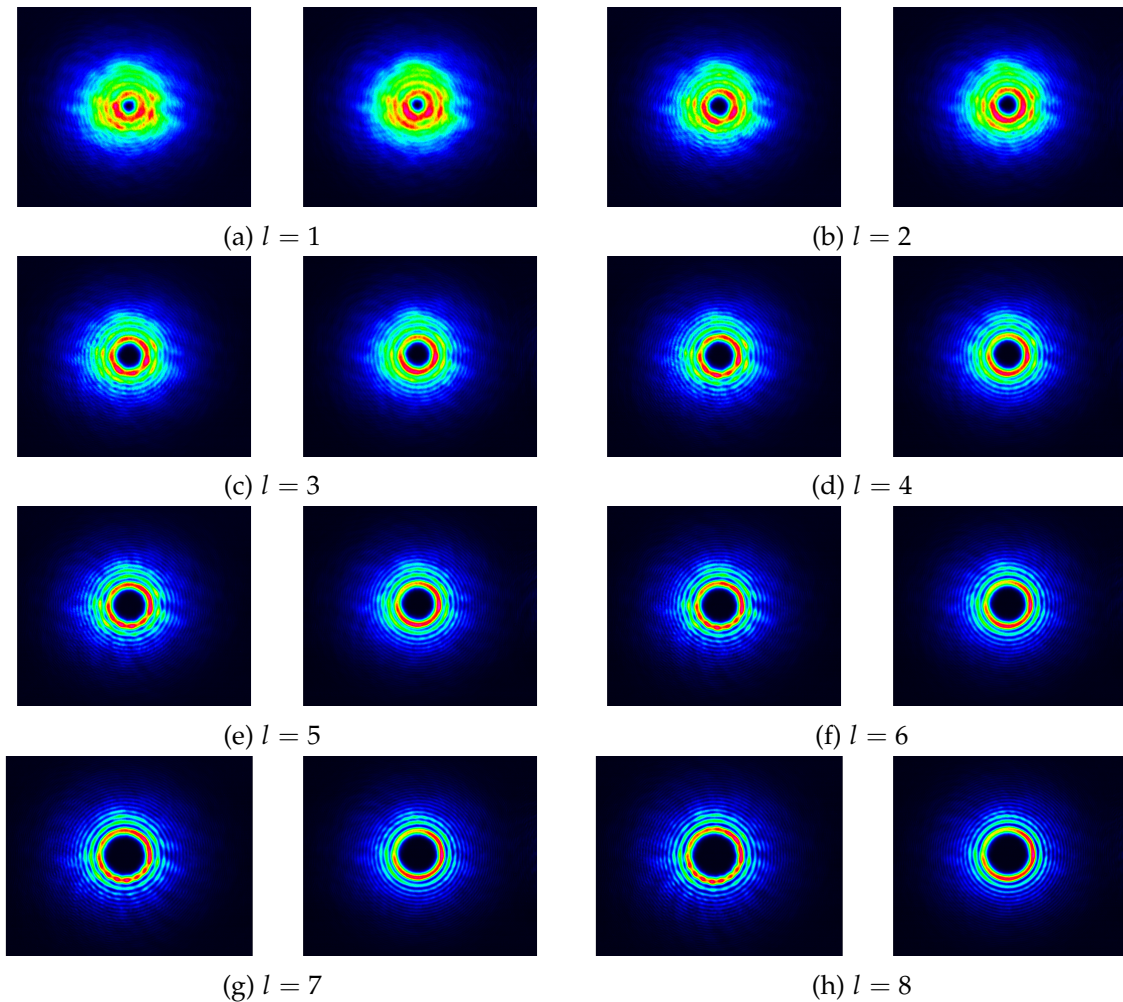
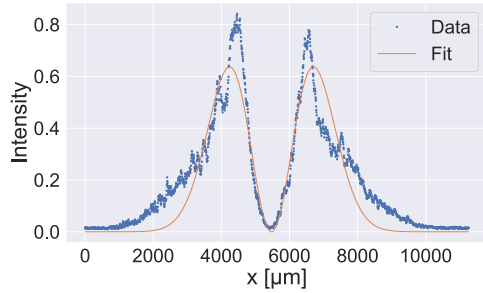
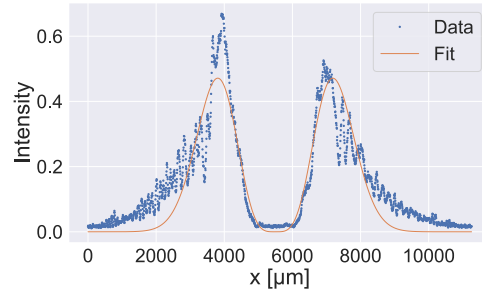


Figure 33: Pictures from the LG modes of different azimuthal orders l captured with the beam profiling camera. The LG modes were generated with the holograms from the *Hamamatsu* software. On the left of each subfigure, a grating with grating number $n = 2$ was used whereas on the right, the grating number is $n = 4$.

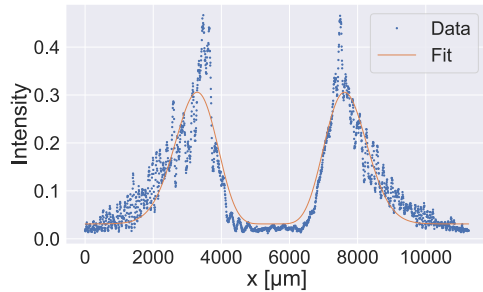
B.2. Plots of the line profiles



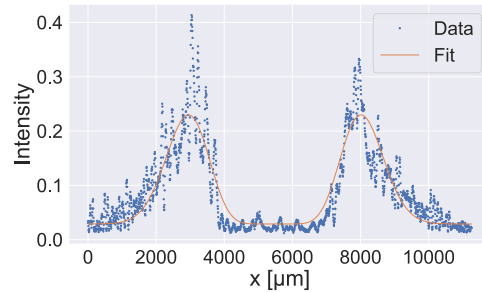
(a) $l = 1$



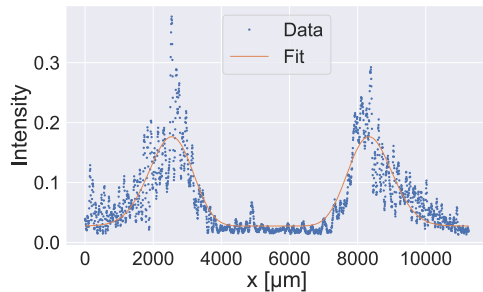
(b) $l = 2$



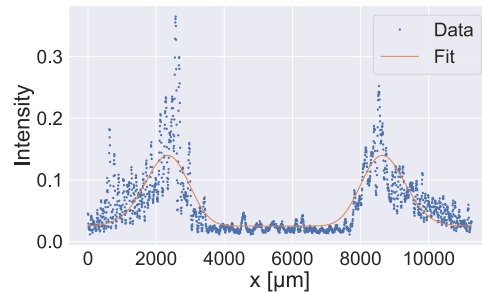
(c) $l = 3$



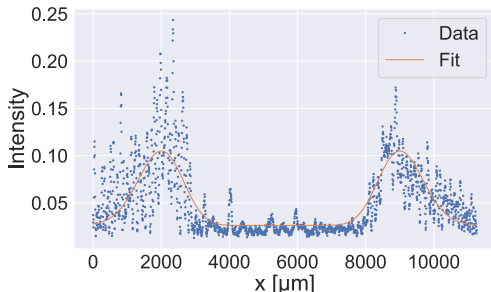
(d) $l = 4$



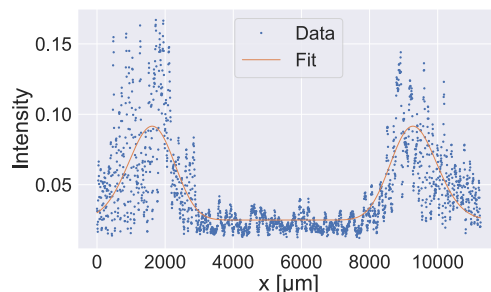
(e) $l = 5$



(f) $l = 6$



(g) $l = 7$



(h) $l = 8$

Figure 34: Plots of the line profiles of the LG modes with different azimuthal orders in x -direction. The holograms to generate the modes were calculated with the implemented algorithm and were combined with a blazed grating of $n = 2$.

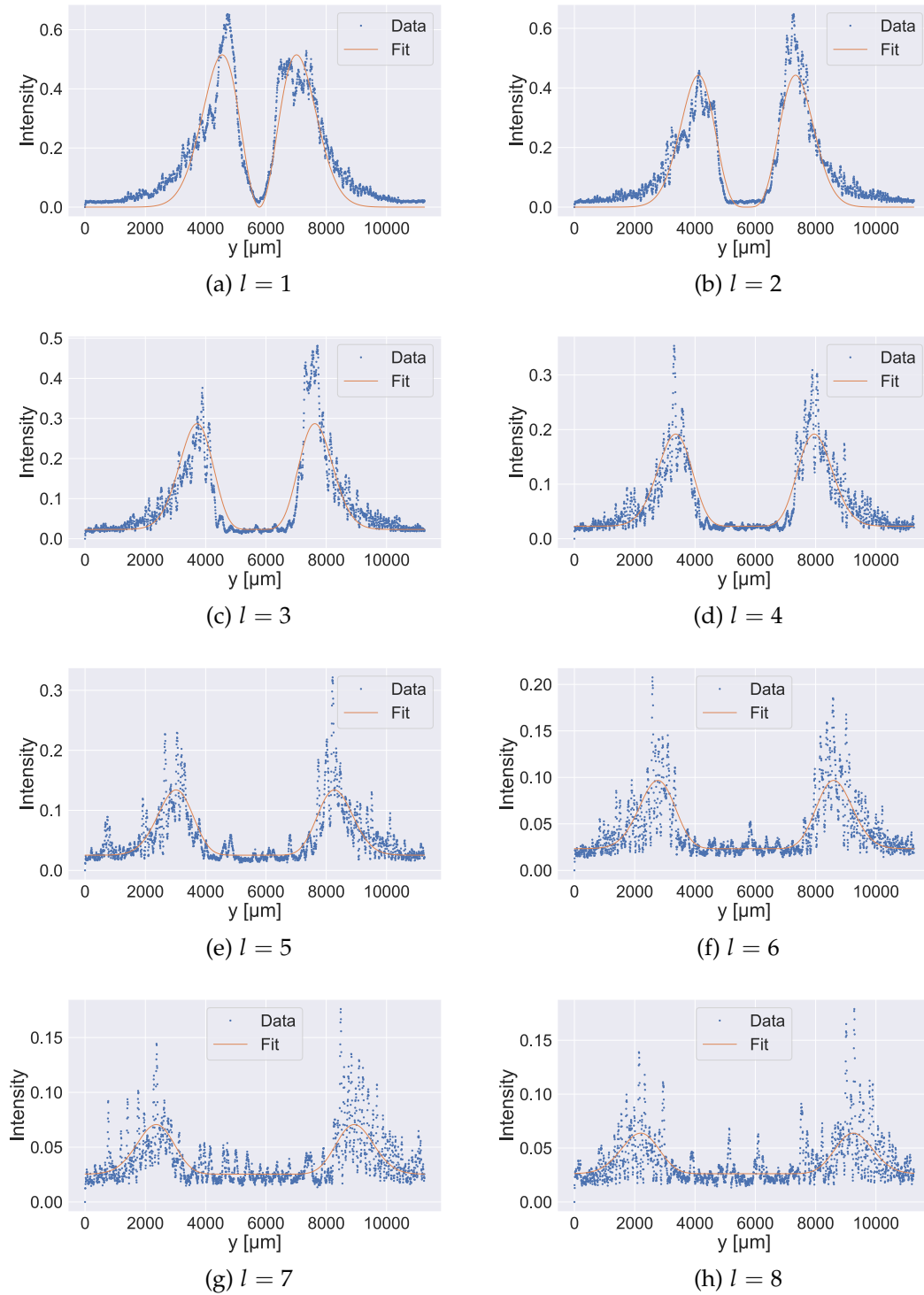


Figure 35: Plots of the line profiles of the LG modes with different azimuthal orders in y -direction. The holograms to generate the modes were calculated with the implemented algorithm and were combined with a blazed grating of $n = 2$.

B.2 Plots of the line profiles

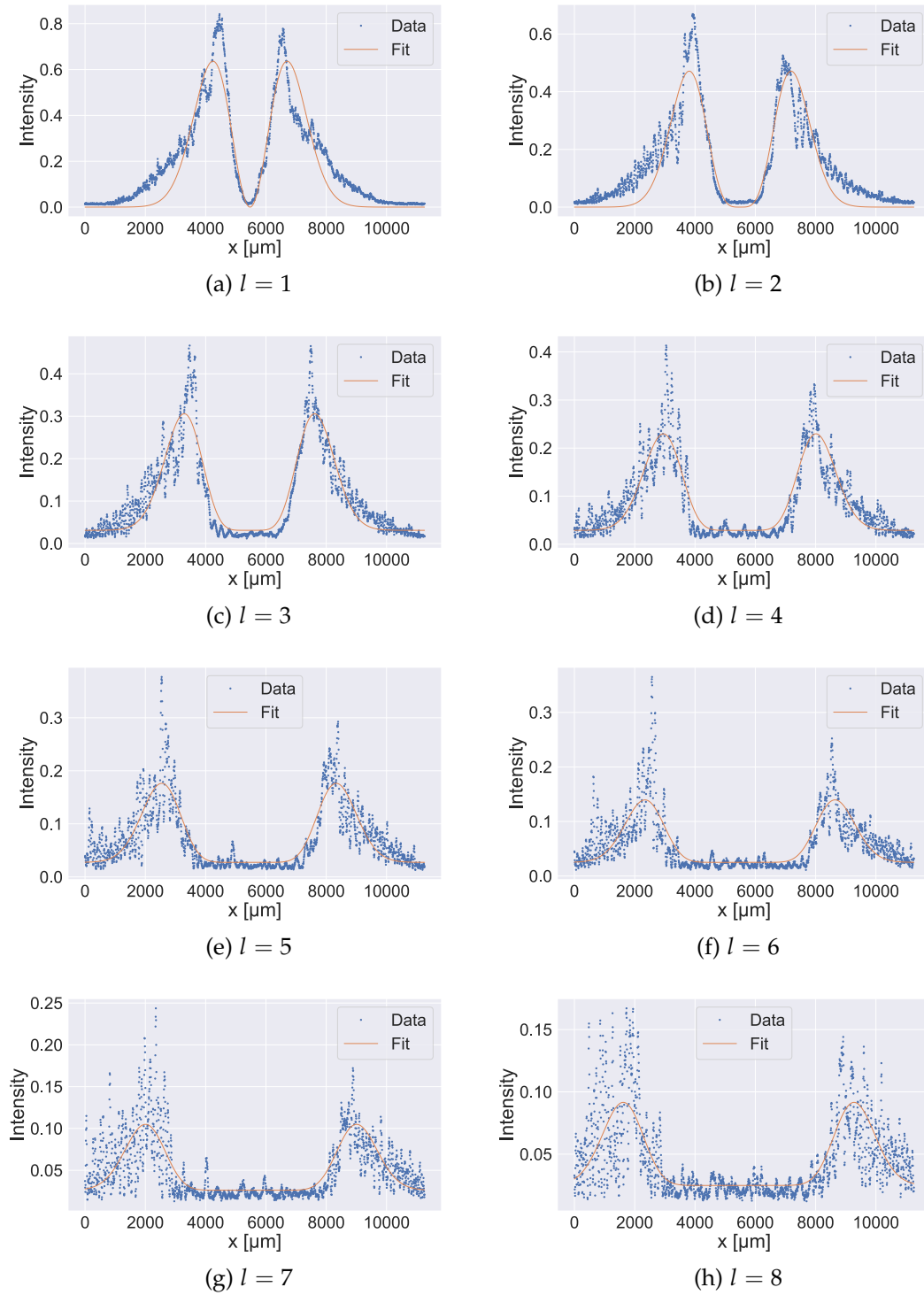


Figure 36: Plots of the line profiles of the LG modes with different azimuthal orders in x -direction. The modes are generated by using the holograms which are calculated by the *Hamamatsu* software. The grating used had a grating number of $n = 2$.

B.2 Plots of the line profiles

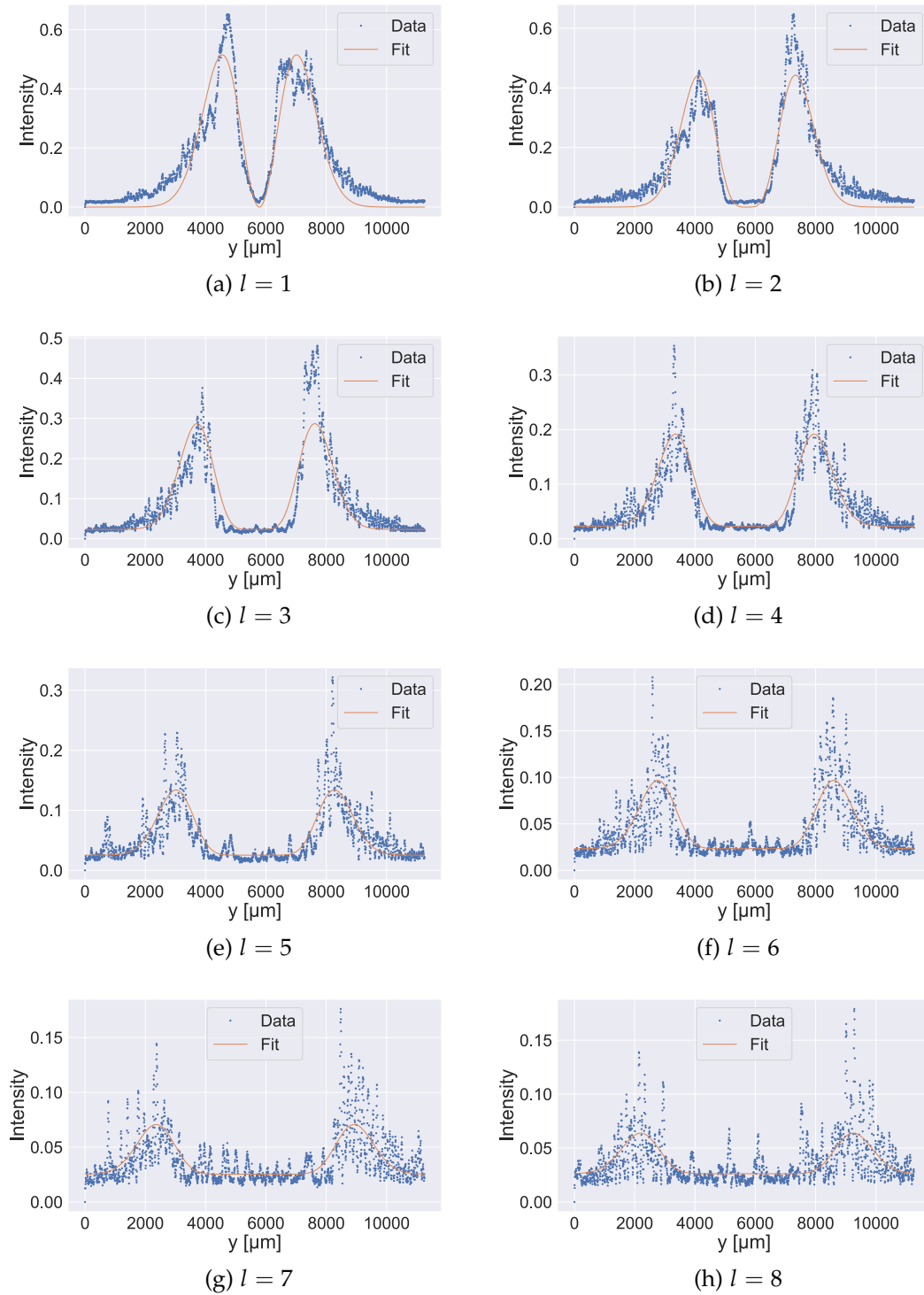


Figure 37: Plots of the line profiles of the LG modes with different azimuthal orders in y -direction. The modes are generated by using the holograms which are calculated by the *Hamamatsu* software. The grating used had a grating number of $n = 2$.

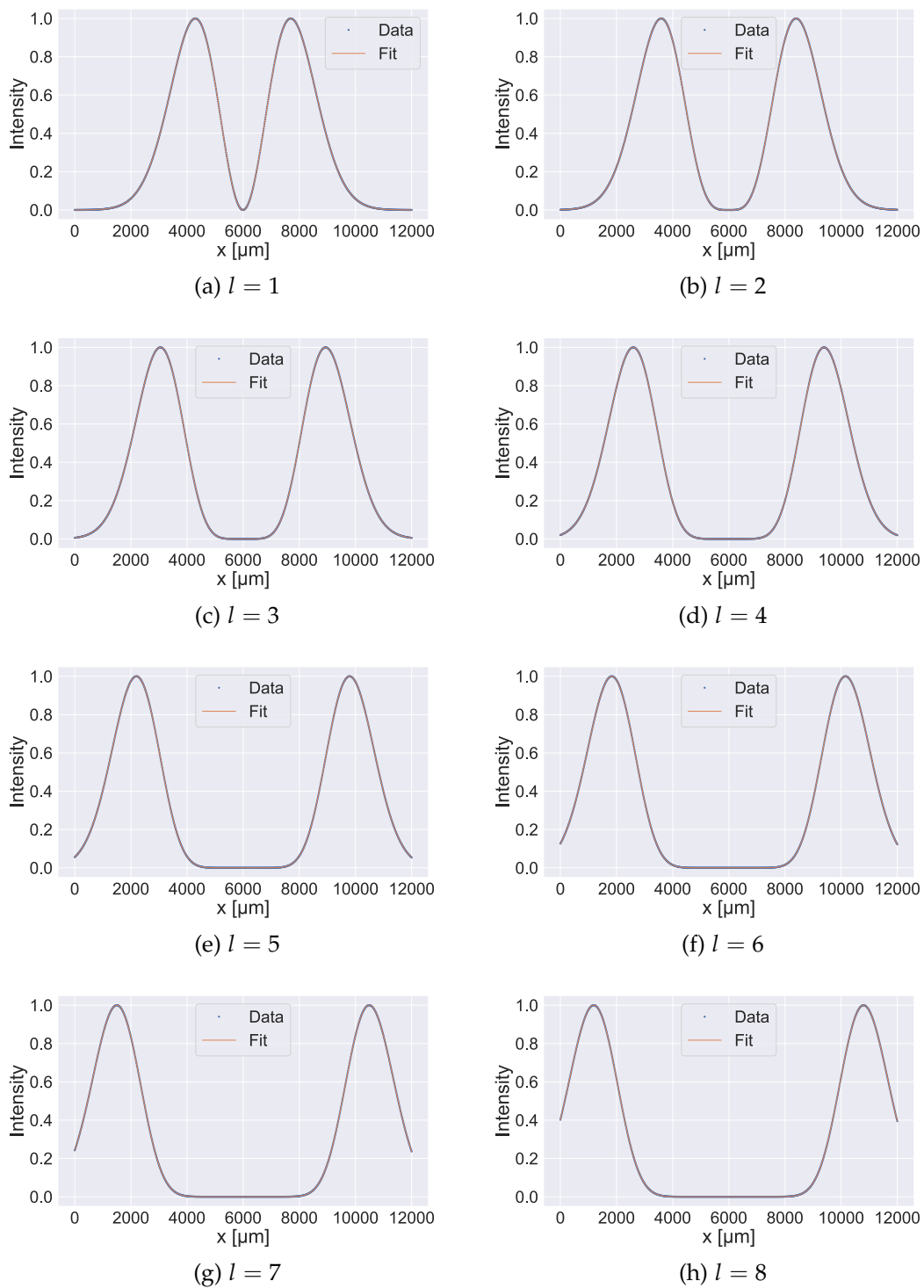


Figure 38: Line profiles of the target beam which is used to calculate the hologram with the phase and amplitude modulating algorithm.

C. Matlab code

```

1 function pattern = amplitude_phase(sz, l, r, N, lambda, varargin)
2
3 % Necessary input arguments:
4 % l = azimuthal mode LG beam,
5 % r = radial mode LG beam of the desired pattern
6 % sz = [sz_y sz_x] size of the patterns in mm or pixels
7 % N = number of iteration
8 % lambda = wavelength of the input beam in mm
9
10 % Optional input arguments:
11 % radius = [radius_y, radius_x] of the incident beam in mm (
    default: [2.98, 3.3] as measured using the knife edge method)
12 % distance = propagation distance in mm of the beam after the
    SLM (default: 600 mm)
13 % sz_unit = either 'mm' or 'pixels': unit of sz (default: mm)
14 % grating = grating number (default: []): it can be either 2 or
    4, adds the grating to the hologram obtained after the last
    iteration
15 % correction = 'on' or 'off' (default: 'on'): adds the
    correction bitmap for lamda = 626nm to the hologram after the
    last iteration
16
17 p = inputParser;
18 p.AddParameter('radius', [2.98, 3.3]);
19 p.AddParameter('distance', 600);
20 p.AddParameter('sz_unit', 'mm');
21 p.AddParameter('grating', []);
22 p.AddParameter('correction', 'on');
23 p.parse(varargin{:});
24
25 assert(numel(p.Results.radius)==2, 'radius must contain two
    elements: radius = [r_y, r_x]');
26
27 % convert size in mm into pixels
28 unit = p.Results.sz_unit;
29 if strcmpi(unit, 'mm')
30     szp = 80*sz;
31 elseif strcmpi(unit, 'pixels')
32     szp = sz;
33 else

```

```

34     error('sz_unit must be either mm or pixels');
35 end
36 assert(szp(2) <= 1272 & szp(1) <= 1024, 'Size of the pattern must
      not exceed the size of the SLM screen 15.9 x 12.8 mm (1272 x
      1024 pixels)');
37
38 z = p.Results.distance;
39
40 % a = input amplitude
41 % Generate a
42 a = otslm.input_pattern(szp, 'radius', p.Results.radius);
43
44
45 % at = desired amplitude pattern
46 % pt = desired phase pattern
47 [pr, at] = otslm.simple.lgmodes(szp, l, r);
48 pt = otslm.tools.finalize(pr); % pr in range -Pi to Pi
49 at = rescale(at);
50
51
52 % Matrix I
53 I = ones(szp);
54
55 % Create S Matrix
56 s1 = ones([ floor(1/2*szp(1)) szp(2) ]);
57 s2 = zeros([ ceil(1/2*szp(1)) szp(2) ]);
58 S = [s1; s2];
59
60 R = I-S;
61
62 % Generate initial random phase
63 p0 = rand(szp);
64 p0 = rescale(p0, -pi, pi);
65
66 % iterations
67
68 for k = 1:N
69
70     f = a.*exp(1i*p0);
71

```

```

72     % Calculate propagation of input beam
73     Uc = otslm.apws(szp, f, lambda, z);
74     ac = abs(Uc);
75     ac = rescale(ac);
76     pc = angle(Uc); % -Pi to Pi
77
78
79     % Calculate plane alpha and beta
80     alpha = otslm.plane(at, pt, ac, pc, S, R);
81     beta = otslm.plane(ac, pc, at, pt, S, R);
82
83     % alpha and beta in the beginning
84     u_alpha = otslm.apws(szp, alpha, lambda, -z);
85     u_beta = otslm.apws(szp, beta, lambda, -z);
86
87     % phase of alpha and beta in the beginning
88     p_alpha = angle(u_alpha); % -Pi to Pi
89     p_beta = angle(u_beta); % -Pi to Pi
90
91     % adding both planes
92     final = exp(1i*p_alpha) + exp(1i*p_beta);
93
94     % New phase pattern
95     p0 = angle(final); % -Pi to Pi
96
97 end
98
99 p0 = rescale(p0, 0, 2*pi);
100
101 % Add zeros to the bounds such that the size of the hologram
    corresponds to
102 % the size of the screen of the SLM (1024 x 1272 pixels); the
    calculated
103 % hologram is centered
104 if szp(1) < 1024
105     x1 = floor((1024-szp(1))/2);
106     x2 = ceil((1024-szp(1))/2);
107     hor1 = zeros([x1 szp(2)]);
108     hor2 = zeros([x2 szp(2)]);
109     p0 = [hor1; p0; hor2];

```

```

110         szp(1) = 1024;
111 end
112 if szp(2) < 1272
113     y1 = floor((1272-szp(2))/2);
114     y2 = ceil((1272-szp(2))/2);
115     vert1 = zeros([szp(1) y1]);
116     vert2 = zeros([szp(1) y2]);
117     p0 = [vert1 p0 vert2];
118 end
119
120 % For generating a bitmap, the phase pattern has to be in the
        range from 0 to 2Pi
121 % Generate the bitmap and save it as 'hologram.bmp'
122
123 pattern = otslm.create_bitmap(p0, 'name', 'hologram.bmp');
124
125 % Add the grating if necessary
126 if isempty(p.Results.grating)
127     % Nothing to do
128 elseif p.Results.grating == 2
129     gr = imread('grating2.bmp');
130     pattern = otslm.combine_bitmaps1({pattern, gr}, 'name', '
        hologram.bmp');
131 elseif p.Results.grating == 4
132     gr = imread('grating4.bmp');
133     pattern = otslm.combine_bitmaps1({pattern, gr}, 'name', '
        hologram.bmp');
134 else
135     error('Grating must be either 2 or 4');
136 end
137
138
139 % Add correction and overwrite 'hologram.bmp' if necessary
140 if strcmpi(p.Results.correction, 'on')
141     correction = imread('correction.bmp');
142     pattern = otslm.combine_bitmaps1({pattern, correction}, '
        name', 'hologram.bmp');
143 elseif strcmpi(p.Results.correction, 'off')
144     % Nothing to do
145 else

```

```

146     error('correction must be either on or off');
147 end
148 end

1 function input_amplitude = input_pattern(sz, varargin)
2 % Necessary input parameter : sz in pixels - sz = [sz_y sz_x]
3
4 % optional parameter: radius - [radius_x, radius_y] in
   millimeters
5
6 p = inputParser;
7 p.AddParameter('radius', [2.98, 3.3]);
8 p.parse(varargin{:});
9 assert(numel(p.Results.radius)==2, 'radius must contain two
   elements: radius = [r_y, r_x]');
10
11 % Converting radius into pixels
12 sg = 80*p.Results.radius;
13 sg = round(sg);
14
15 % Generate the grid (0 at the center)
16 [X,Y] = otslm.simple.grid(sz);
17
18 % Creating a Gaussian amplitude pattern
19 input_amplitude = sqrt(exp(-2*X.^2/(sg(2)^2)).*exp(-2*Y.^2/(sg
   (1)^2)));
20
21 end

1 function pattern = apws(sz, beam, lambda, z)
2 % This function propagates the beam using the angular plane wave
   spectrum
3 % method (APWS).
4
5 % Necessary input arguments:
6 % sz = [sz_y sz_x]: size of the beam/screen in pixels
7 % beam = amplitude*exp(i*phase): beam that should be propagated
8 % lambda: wavelength in nm of the beam
9 % z: propagation distance in mm (-z for backward propagation)
10

```

```

11 % Calculate the discrete Fourier transform of the complex
    amplitude of the beam
12 y = fft2(beam, sz(1), sz(2));
13 y = fftshift(y);
14
15 % Calculate length of the hologram in x and y direction
16 ly = sz(1)/80; % size in mm
17 lx = sz(2)/80; % size in mm
18
19 % Calculate angular wave number in x and y direction
20 kx = linspace((-pi*(sz(2)/2)/(lx/2)), (pi*(sz(2)/2)/(lx/2)), sz
    (2));
21 ky = linspace((-pi*(sz(1)/2)/(ly/2)), (pi*(sz(1)/2)/(ly/2)), sz
    (1));
22
23 % Generate a meshgrid of wave numbers
24 [kx, ky] = meshgrid(kx, ky);
25
26 % Calculate k in z direction
27 ph = sqrt((2*pi/(lambda*10-6))^2 - kx.^2 - ky.^2);
28
29 % calculate the complex amplitude of the beam
30 e = exp(1i*z*ph);
31 h = y.*e;
32
33 % return inverse Fourier transform
34 pattern = ifft2(ifftshift(h));
35
36 end

1 function pattern = plane(as, ps, ar, pr, S, R)
2 % This function returns the alpha and beta plane.
3 % as = amplitude that should be multiplied with matrix S (alpha:
    target,
4 %     beta: calculated)
5 % ps = phase that should be multiplied with matrix S (alpha:
    target, beta:
6 %     calculated)
7 % ar = amplitude that should be multiplied with matrix R = (I-S)
    (alpha:

```

```

8 %      calculated , beta: target)
9 % pr = phase that should be multiplied with matrix R = (I-S) (
      alpha:
10 %      calculated , beta: target)
11
12 a = as.*S + ar.*R;
13 p = ps.*S + pr.*R;
14 pattern = a.*exp(1i*p);
15 end

1 function pattern = create_bitmap(phase, varargin)
2 % input: phase = phase pattern in the range from 0 to 2Pi
3 %      name = name of the file as which the bitmap should be
      saved , e. g. 'file.bmp'
4 % output: pattern = bitmap
5
6 p = inputParser;
7 p.AddParameter('name', [])
8 p.parse(varargin{:})          % shifts the phase pattern into the
      range 0 to 2Pi
9 pattern1 = 194/(2*pi).*phase;          % sets 2Pi to 194
10 pattern = uint8(pattern1);          % rounds the values to
      uint8 values
11
12 file = p.Results.name;
13 if isempty(file)
14     % Nothing to do
15 else
16     imwrite(pattern , file)          % saves the bitmap
17 end
18 end

1 function bitmap = combine_bitmaps1(x, varargin)
2 % This function combines a variable number of bitmaps.
3 % input: cell array x = {bitmap1, bitmap2, ...} containing the
      bitmaps that need to be combined
4 % output: bitmap of the combined input bitmaps
5
6 p = inputParser;
7 p.AddParameter('name', [])
8 p.parse(varargin{:})

```

```
9
10
11 a = zeros(size(x{1}));
12 for i = 1:numel(x)
13     a = a + double(x{i});
14 end
15 b = mod(a, 194);
16 bitmap = uint8(b);
17
18 file = p.Results.name;
19 if isempty(file)
20     % Nothing to do
21 else
22     imwrite(bitmap, file)           % saves the bitmap if
                                     desired
23 end
24 end
```

References

- [1] I. N. Bronstein and K. A. Semendjajew. *Taschenbuch der Mathematik*. Ed. by V. Ziegler G. Grosche and D. Ziegler. Frankfurt/Main: Verlag Harri Deutsch Thun, 1989.
- [2] Rosales-Guzmán Carmelo and Forbes Andrew. *How to Shape Light with Spatial Light Modulators*. Society of Photo-Optical Instrumentation Engineers (SPIE), 2017. URL: <https://ebookcentral.proquest.com/lib/umainz/detail.action?docID=4947383>.
- [3] *Das konfokale Laser Scanning Mikroskop (LSM)*. URL: https://www.dlr.de/wf/desktopdefault.aspx/tabid-10023/17102_read-41398/ (visited on 08/25/2021).
- [4] Wolfgang Demtröder. *Experimentalphysik 3 - Atome, Moleküle und Festkörper*. 7th ed. Springer Spektrum, 2017.
- [5] Wolfgang Demtröder. *Laserspektroskopie - Grundlagen und Techniken*. 5th ed. Springer-Verlag Berlin Heidelberg, 2007. DOI: 10.1007/978-3-540-33793-5.
- [6] Jof Enriquez. *Twisting Light Using Two Spatial Degrees Of Freedom Could Solve Spectrum Crunch*. URL: <https://www.photonicsonline.com/doc/twisting-light-using-two-spatial-degrees-of-freedom-could-solve-spectrum-crunch-0001> (visited on 08/30/2021).
- [7] *Formelsammlung zur Vorlesung Auswertung von Messungen und Fehlerrechnung*. Universität Würzburg. URL: https://www.physik.uni-wuerzburg.de/fileadmin/physik-grundpraktikum/_imported/fileadmin/11016800/Modulbeschreibungen/Fehlerrechnung/Formelsammlung.pdf.
- [8] Enrique J. Galvez. *Gaussian Beams*. Department of Physics and Astronomy, Colgate University, 2009.
- [9] Joseph W. Goodman. *Introduction to Fourier optics*. New York: W. H. Freeman and Company, 2017.
- [10] Hamamatsu. *LCOS-SLM X15213 Series Operation manual*.
- [11] Jullien, Aurélie. "Spatial light modulators". In: *Photoniques* 101 (2020), pp. 59–64. DOI: 10.1051/photon/202010159. URL: <https://doi.org/10.1051/photon/202010159>.
- [12] Patrick Kaspar. "Aufbau und Charakterisierung eines frequenzverdoppelten Lasersystems für die "Zwei-Photonen Rydberg-Anregung von Rubidium". Bachelor thesis. Universität Stuttgart, 2015.

- [13] Shlomit Katz, Natan Kaplan, and Israel Grossinger. "Using Diffractive Optical Elements: DOEs for beam shaping - fundamentals and applications". In: *Laser Technik Journal* 15 (Oct. 2018), pp. 29–32. DOI: 10.1002/latj.201800021.
- [14] Sander Konijnenberg. *Basic optics*. URL: https://www.youtube.com/playlist?list=PLG6kLm-LDbADtYL_Hns29b13Rxxv0erj7k (visited on 08/24/2021).
- [15] Isaac C.D. Lenton et al. "OTSLM toolbox for Structured Light Methods". In: *Computer Physics Communications* 253 (2020), p. 107199. ISSN: 0010-4655. DOI: <https://doi.org/10.1016/j.cpc.2020.107199>. URL: <https://www.sciencedirect.com/science/article/pii/S0010465520300412>.
- [16] Naoya Matsumoto et al. "Generation of high-quality higher-order Laguerre-Gaussian beams using liquid-crystal-on-silicon spatial light modulators". In: *J. Opt. Soc. Am. A* 25.7 (July 2008), pp. 1642–1651. DOI: 10.1364/JOSAA.25.001642. URL: <http://josaa.osa.org/abstract.cfm?URI=josaa-25-7-1642>.
- [17] William D. Phillips. "Nobel Lecture: Laser cooling and trapping of neutral atoms". In: *Rev. Mod. Phys.* 70 (3 July 1998), pp. 721–741. DOI: 10.1103/RevModPhys.70.721. URL: <https://link.aps.org/doi/10.1103/RevModPhys.70.721>.
- [18] Salla Gangi Reddy et al. "Divergence of optical vortex beams". In: *Appl. Opt.* 54.22 (Aug. 2015), pp. 6690–6693. DOI: 10.1364/AO.54.006690. URL: <http://ao.osa.org/abstract.cfm?URI=ao-54-22-6690>.
- [19] Stefan Roth and Achim Stahl. *Optik*. Springer Spektrum, 2019.
- [20] Yijie Shen et al. "Optical vortices 30 years on: OAM manipulation from topological charge to multiple singularities". In: *Light: Science & Applications* 8.1, 90 (Oct. 2019), p. 90. DOI: 10.1038/s41377-019-0194-2.
- [21] N. Simpson, Les Allen, and Miles Padgett. "Optical tweezers and optical spanners with Laguerre-Gaussian modes". In: *Journal of Modern Optics* 43 (Aug. 1996), pp. 2485–2492. DOI: 10.1080/095003496154392.
- [22] Norbert Straumann. *Quantenmechanik - Ein Grundkurs über nichtrelativistische Quantentheorie*. 2nd ed. Springer-Verlag Berlin Heidelberg, 2013. DOI: 10.1007/978-3-642-32175-7.
- [23] Orazio Svelto. *Principles of Lasers*. 4th ed. Springer Verlag, 1998.
- [24] Shaohua Tao and Weixing Yu. "Beam shaping of complex amplitude with separate constraints on the output beam". In: *Opt. Express* 23.2 (Jan. 2015), pp. 1052–1062. DOI: 10.1364/OE.23.001052. URL: <http://www.opticsexpress.org/abstract.cfm?URI=oe-23-2-1052>.

- [25] Erik H. Waller and Georg von Freymann. "Independent spatial intensity, phase and polarization distributions". In: *Opt. Express* 21.23 (Nov. 2013), pp. 28167–28174. DOI: 10.1364/OE.21.028167. URL: <http://www.opticsexpress.org/abstract.cfm?URI=oe-21-23-28167>.
- [26] Jing Pan Wen-Kai Shao Yuan He. "Some identities for the generalized Laguerre polynomials". In: 9.5 (2016), pp. 3388–3396. ISSN: ISSN 2008-1901. DOI: 10.22436/jnsa.009.05.124. URL: <http://dx.doi.org/10.22436/jnsa.009.05.124>.
- [27] Liang Wu, Shubo Cheng, and Shaohua Tao. "Simultaneous shaping of amplitude and phase of light in the entire output plane with a phase-only hologram". In: *Scientific Reports* 5 (Oct. 2015). DOI: 10.1038/srep15426.